Mon. Not. R. Astron. Soc. **000**, 1–?? (2012) Printed 19 April 2013 (MN LaTeX style file v2.2)

arXiv:1304.5136v1 [astro-ph.GA] 18 Apr 2013

Properties of dense cores in clustered massive star-forming regions at high angular resolution

Álvaro Sánchez-Monge[1,2]*, Aina Palau[3], Francesco Fontani[1], Gemma Busquet[4], Carmen Juárez[3,2], Robert Estalella[2], Jonathan C. Tan[5], Inma Sepúlveda[2], Paul T. P. Ho[6,7], Qizhou Zhang[7] and Stan Kurtz[8]

[1] *Osservatorio Astrofisico di Arcetri, INAF, Largo Enrico Fermi 5, I-50125, Firenze, Italy*
[2] *Dpt. d'Astronomia i Meteorologia (IEEC-UB), ICC, Universitat de Barcelona, Martí i Franquès 1, E-08028, Barcelona, Spain*
[3] *Institut de Ciències de l'Espai (CSIC-IEEC), Campus UAB, Facultat de Ciències, Torre C-5p, E-08193 Bellaterra, Barcelona, Spain*
[4] *INAF-Istituto di Astrofisica e Planetologia Spaziali, Via Fosso del Cavaliere 100, I-00133 Roma, Italy*
[5] *Dpts. of Astronomy & Physics, University of Florida, Gainesville, FL 32611, USA*
[6] *Institute of Astronomy and Astrophysics, Academia Sinica, P.O. Box 23-141, Taipei 106, Taiwan*
[7] *Harvard-Smithsonian Center for Astrophysics, 60 Garden Street, Cambridge, MA 02138, USA*
[8] *Centro de Radioastronomía y Astrofsica, Universidad Nacional Autónoma de México, P.O. Box 3-72, 58090, Morelia, Mich., Mexico*

Accepted date. Received date; in original form date

ABSTRACT

We aim at characterising dense cores in the clustered environments associated with intermediate/high-mass star-forming regions. For this, we present an uniform analysis of Very Large Array NH_3 (1,1) and (2,2) observations towards a sample of 15 intermediate/high-mass star-forming regions, where we identify a total of 73 cores, classify them as protostellar, quiescent starless, or perturbed starless, and derive some physical properties. The average sizes and ammonia column densities of the total sample are ~ 0.06 pc and $\sim 10^{15}$ cm^{-2}, respectively, with no significant differences between the starless and protostellar cores, while the linewidth and rotational temperature of quiescent starless cores are smaller, ~ 1.0 km s^{-1} and 16 K, than linewidths and temperatures of protostellar (~ 1.8 km s^{-1} and 21 K), and perturbed starless (~ 1.4 km s^{-1} and 19 K) cores. Such linewidths and temperatures for these quiescent starless cores in the surroundings of intermediate/high-mass stars are still significantly larger than the typical linewidths and rotational temperatures measured in starless cores of low-mass star-forming regions, implying an important non-thermal component. We confirm at high angular resolutions (spatial scales ~ 0.05 pc) the correlations previously found with single-dish telescopes (spatial scales $\gtrsim 0.1$ pc) between the linewidth and the rotational temperature of the cores, as well as between the rotational temperature and the linewidth with respect to the bolometric luminosity. In addition, we find a correlation between the temperature of each core and the incident flux from the most massive star in the cluster, suggesting that the large temperatures measured in the starless cores of our sample could be due to heating from the nearby massive star. A simple virial equilibrium analysis seems to suggest a scenario of a self-similar, self-graviting, turbulent, virialised hierarchy of structures from clumps (~ 0.1–10 pc) to cores (~ 0.05 pc). A closer inspection of the dynamical state taking into account external pressure effects, reveal that relatively strong magnetic field support may be needed to stabilise the cores, or that they are unstable and thus on the verge of collapse.

Key words: ISM: molecules – radio lines: ISM – stars: formation – stars: early-type.

1 INTRODUCTION

The initial conditions of the star formation process in clusters are still poorly understood. Studies have unveiled the

---

* E-mail: asanchez@arcetri.astro.it (ASM)

Table 1. Massive star-forming regions observed in NH_3 with the Very Large Array, and few observational and derived parameters

Region[a]	d (kpc)	$L_{\rm bol}$ ($L_\odot$)	VLA project	Phase centre[b]		Synthesised beam[c]		RMS[d]	Clumpfind[e]		
				R.A.	Dec.	HPBW	P.A.		P	B	S
1. 00117+6412	1.8	1300	AB1217	00:14:27.725	+64:28:46.17	3.9 × 3.5	+46	2.2	66	35	10
2. AFGL5142	1.8	2200	AZ120[f]	05:30:48.024	+33:47:54.44	3.6 × 2.6	−14	3.5	203	20	10
3. 05345+3157NE	1.8	630	AF471	05:37:52.400	+32:00:06.00	2.3 × 2.3	+92	1.4	39	25	5
4. 05358+3543NE	1.8	3100	AC733	05:39:12.600	+35:45:52.30	5.8 × 4.1	+53	5.3	269	40	10
5. 05373+2349	1.6	1100	AF484	05:40:24.500	+23:50:55.00	3.1 × 2.2	−73	4.0	116	30	10
6. 19035+0641	2.2	7700	AF386	19:06:01.610	+06:46:35.80	4.0 × 3.7	−13	2.6	378	28	10
7. 20081+3122	2.5	28200	AF386	20:10:09.050	+31:31:35.20	5.0 × 4.4	−56	3.3	602	25	5
8. 20126+4104	1.64	8900	AZ113	20:14:26.053	+41:13:31.49	3.6 × 3.2	+10	3.8	873	20	10
9. G75.78+0.34	3.8	96000	AF386	20:21:43.970	+37:26:38.10	3.7 × 3.4	−57	3.8	181	30	5
10. 20293+3952	2.0	8000	AZ120	20:31:10.698	+40:03:10.75	6.9 × 3.1	+72	3.0	240	40	10
11. 20343+4129	1.4	1500	AS708	20:36:07.301	+41:39:57.20	4.2 × 3.2	+11	3.5	224	27	10
12. 22134+5834	2.6	11800	AK558	22:15:08.099	+58:49:10.00	3.8 × 3.1	+88	1.5	31	40	10
13. 22172+5549N	2.4	830	AF484	22:19:08.600	+56:05:02.00	3.2 × 3.0	+17	1.2	61	30	10
14. 22198+6336	0.76	340	AS926[f]	22:21:26.764	+63:51:37.89	3.7 × 3.1	−41	3.8	61	40	10
15. CepA	0.7	25000	AF386	22:56:17.870	+62:01:48.60	5.4 × 4.9	−29	3.6	332	30	6

[a] Name of regions starting with numbers (e. g., 00117+6412) refer to the IRAS name (Neugebauer et al. 1984).

[b] Phase centre coordinates (in Equatorial J2000.0) of the ammonia maps. Right ascension in units h:m:s and Declination in units d:m:s.

[c] Synthesised beam (HPBW) in arcsec, and position angle (P.A.) in degrees.

[d] RMS noise level, in units of mJy beam^{-1}, per channel (of 0.3 km s^{-1} or 0.6 km s^{-1}; see Table 2).

[e] P: intensity peak (in mJy km s^{-1}) of the zero-order moment map. B (bottom) and S (step) parameters, in percentage of the peak, used in the Clumpfind algorithm to extract the position of the cores (see Sect. 3.1).

[f] AFGL5142 and 22198+6336 includes also data of the project AZ114.

physical and chemical properties of starless *isolated low-mass* cores on the verge of gravitational collapse in nearby low-mass star-forming regions, showing that they have dense ($n \sim 10^5$–10^6 cm^{-3}) and cold ($T \sim 10$ K) nuclei (e. g., Tafalla et al. 2002, 2004; Schnee et al. 2010), and that the internal motions are thermally dominated, as demonstrated by their close-to-thermal linewidths, even when observed at low angular resolution (see Bergin & Tafalla 2007, for a review). In the cold and dense nuclei of these cores, C-bearing molecular species such as CO and CS are strongly depleted (e. g., Caselli et al. 2002; Tafalla et al. 2002), while N-bearing species such as N_2H^+ and NH_3 maintain large abundances in the gas phase (e. g., Caselli et al. 2002; Crapsi et al. 2005).

One major issue that has so far been poorly investigated is if, and how, the environment influences the physical and chemical properties of these pre–stellar cores. In clusters containing several forming stars in a small volume (of diametre $\leqslant 0.1$ pc), turbulence, relative motions, and interaction with nearby forming (proto-)stars can affect the less evolved condensations (e. g., Ward-Thompson et al. 2007). Such an interaction is expected to be much more important in clusters containing *intermediate-/high-mass protostars* or newly formed massive stars, given the typical energetic feedback associated with the earliest stages of massive star formation (powerful outflows, strong winds, expanding HII regions) and the high pressure of the parental pc-scale clumps. There is also vigorous theoretical debate on how star formation proceeds in clustered regions. Specifically: are the local kinematics of the gas dominated by feedback from protostellar outflows of already-forming, generally low-mass stars or from feedback from high-mass stars (Nakamura & Li 2007)? Can a model of star formation starting from quiescent starless cores, which has been successfully developed to explain observations of regions of isolated low-mass star formation, be applied to clustered regions (McKee & Tan 2003)? To constrain theoretical models, it is crucial to measure the main physical and chemical properties of starless and star-forming cores in clustered environments.

An observational effort in this direction has started, but it is mostly concentrated on nearby low-mass star-forming regions like Ophiuchus (e. g., André et al. 2007; Friesen et al. 2009) and Perseus (e. g., Foster et al. 2009), due to the fact that the typical large distances ($\geqslant 1$ kpc) of high-mass star-forming regions make the study of clustered environments very challenging. Foster et al. (2009) and Friesen et al. (2009) show that starless cores (studied at spatial scales ~ 0.01–0.05 pc) within low-mass star-forming clusters have typically higher kinetic temperatures (~ 13–14 K) than low-mass isolated cores (~ 10 K). On the other hand, the kinematics of these low-mass protoclusters seem to be dominated by thermal motions like in more isolated cores, even though the external environment is turbulent (André et al. 2007). On the contrary, in the very few published studies of (proto-)clusters containing an intermediate-/high-mass forming star, the internal motions of starless cores are dominated by turbulence (e. g., Fontani et al. 2008, 2009 for IRAS 05345+3157; Wang et al. 2008 for G28.34+0.06; Pillai et al. 2011 for G29.96−0.02 and G35.20−1.74; Fontani et al. 2012b for IRAS 20343+4129).

By using ammonia, Palau et al. (2007b) measured the temperature of the starless cores in the high-mass protocluster IRAS 20293+3952 at spatial scales of ~ 0.05 pc, through Very Large Array observations of the NH_3 (1,1) and (2,2) inversion transitions. In fact, NH_3 is the ideal thermometer for cold and dense gas because it is produced by the volatile molecular nitrogen, which is not expected to freeze out even in very cold and dense gas, and the NH_3 (2,2) to (1,1) line ratio is sensitive to temperature (e. g.,

Table 2. Configurations used, epochs, calibrators and spectral setup of the Very Large Array observational projects

Project	VLA config.	Epoch of observation		Flux calibrator	Gain calibrators (Bootstrapped fluxes, Jy)		Bandwidth (MHz)	Spectral resolution	
								(kHz)	(km s^{-1})
AB1217	D	2007	May	3C286,3C48	J0102+584	3.85 ± 0.06	3.125	48.8	0.6
AC733	DnC	2004	Jun	3C84	J0530+135	3.33 ± 0.02	3.125	48.8	0.6
AF386	D	2001	Jan	3C286	J2025+337	2.50 ± 0.04	3.125	48.8	0.6
					J1849+005	0.81 ± 0.01			
					J2322+509	0.72 ± 0.01			
AF471	D	2009	Oct/Nov	3C286,3C48	J0555+398	3.15 ± 0.01	3.125	24.4	0.3
AF484	D	2009	Oct/Nov	3C48	J0559+238	0.80 ± 0.01	3.125	24.4	0.3
					J2148+611	0.63 ± 0.01			
AK558	D	2003	May	3C286	J2148+611	0.60 ± 0.01	3.125	48.8	0.6
AS708	C	2001	Jul	3C286	J2015+371	2.34 ± 0.04	3.125	48.8	0.6
AS926	C	2008	Apr	3C286,3C48	J2146+611	0.72 ± 0.02	3.125	48.8	0.6
AZ113	D	1999	May	3C286,3C48	J2013+370	2.27 ± 0.21	3.125	24.4	0.3
AZ114	D	1999	Mar	3C48	J2230+697	0.43 ± 0.01	3.125	48.8	0.6
					J0552+398	3.46 ± 0.05			
AZ120	C	2000	Apr	3C48	J0552+398	4.72 ± 0.15	3.125	48.8	0.6
	D	2000	Sep	3C48	J0552+398	3.38 ± 0.04			
					J2015+371	3.84 ± 0.02			

Ho & Townes 1983). Moreover, because other volatile species (like N_2H^+) cannot be used to derive the temperature, *ammonia is the unique tracer for this purpose.* Palau et al. (2007b) found temperatures of 16 K for starless cores in IRAS 20293+3952, i. e., higher than those measured in isolated low-mass starless cores (or infrared dark clouds with no active star formation; e. g., Ragan et al. 2011), but similar to the values measured in active clustered cores in Perseus and Ophiuchus.

In this paper, we study a sample of 15 massive star-forming regions (see Table 1) observed with the Very Large Array (providing an average spatial resolution of ~ 0.05 pc) and analysed them in an uniform way. The main goal is to understand whether the results obtained in the few examples shown above are also obtained when analysing a statistically significant sample. The regions were selected according to the following criteria: i) regions must be at distances $\lesssim 3.5$ kpc, to obtain spatial resolution $\lesssim 0.05$ pc, similar to the scale of the cores (0.03–0.2 pc: e. g., Bergin & Tafalla 2007); ii) regions must have bolometric luminosities larger than $\sim 300\ L_\odot$, which are the luminosities where clustering seems to be important (e. g., Testi et al. 1999; Palau et al. 2013); and iii) regions must be still associated with important amounts of gas and dust judging from single-dish observations of dust and molecular gas studies (e. g., Molinari et al. 1996; Beuther et al. 2002b).

2 OBSERVATIONS

The Very Large Array (VLA[1]) was used to observe the ammonia (J,K) = (1,1) and (2,2) inversion transitions toward 15 intermediate/high-mass star-forming regions. These observations are part of different observational projects carried out on different epochs (from 1999 to 2009), and with the array in compact configurations (C, DnC or D). In Table 1 we list the 15 massive star-forming regions, indicating the name of the VLA project and the coordinates of the phase centre for each region. More technical details of each observational project, such as calibrators and epochs, are provided in Table 2. The full-width at half-maximum of the primary beam at the frequency of the observations (~ 23.7 GHz) is approximately 2 arcmin. The spectral setup configuration used in each project (i. e., bandwidth and spectral resolution) are indicated in Table 2. The absolute flux scale was set by observing the quasars 1331+305 (3C286), 0137+331 (3C48) or 0319+415 (3C84), for which we adopted a flux of 2.41 Jy, 1.05 Jy and 16 Jy, respectively. Gain-calibration was done against nearby quasars, which were typically observed at regular time intervals of $\sim$ 5–10 minutes before and after each target observation. Flux calibration errors could be of up to 20–30%. The data reduction followed the VLA standard guidelines for calibration of high-frequency data, using the NRAO package AIPS. Final images were produced with the task IMAGR of AIPS, with the robust parameter of Briggs (1995) typically set to 5, corresponding to natural weighting. Two sources (AFGL 5142 and 22198+6336) were observed in different projects with different angular resolutions. For these sources we combined the *uv*-data to improve the sensitivity and *uv*-coverage of the final images. The resulting synthesised beams and rms noise levels (per channel) are indicated in Table 1.

3 RESULTS AND ANALYSIS

3.1 Core identification and classification

In Fig. 1, we present the zero-order moment (velocity-integrated intensity) maps of the NH_3 (1,1) emission for the 15 massive star-forming regions studied in this work, while in Fig. B1, we present the first-order (intensity weighted mean $v_{\rm LSR}$) and second-order (intensity weighted mean velocity linewidth) moment maps. The zero-order moment

---

[1] The Very Large Array is operated by the National Radio Astronomy Observatory (NRAO). The NRAO is a facility of the National Science Foundation operated under cooperative agreement by Associated Universities, Inc.

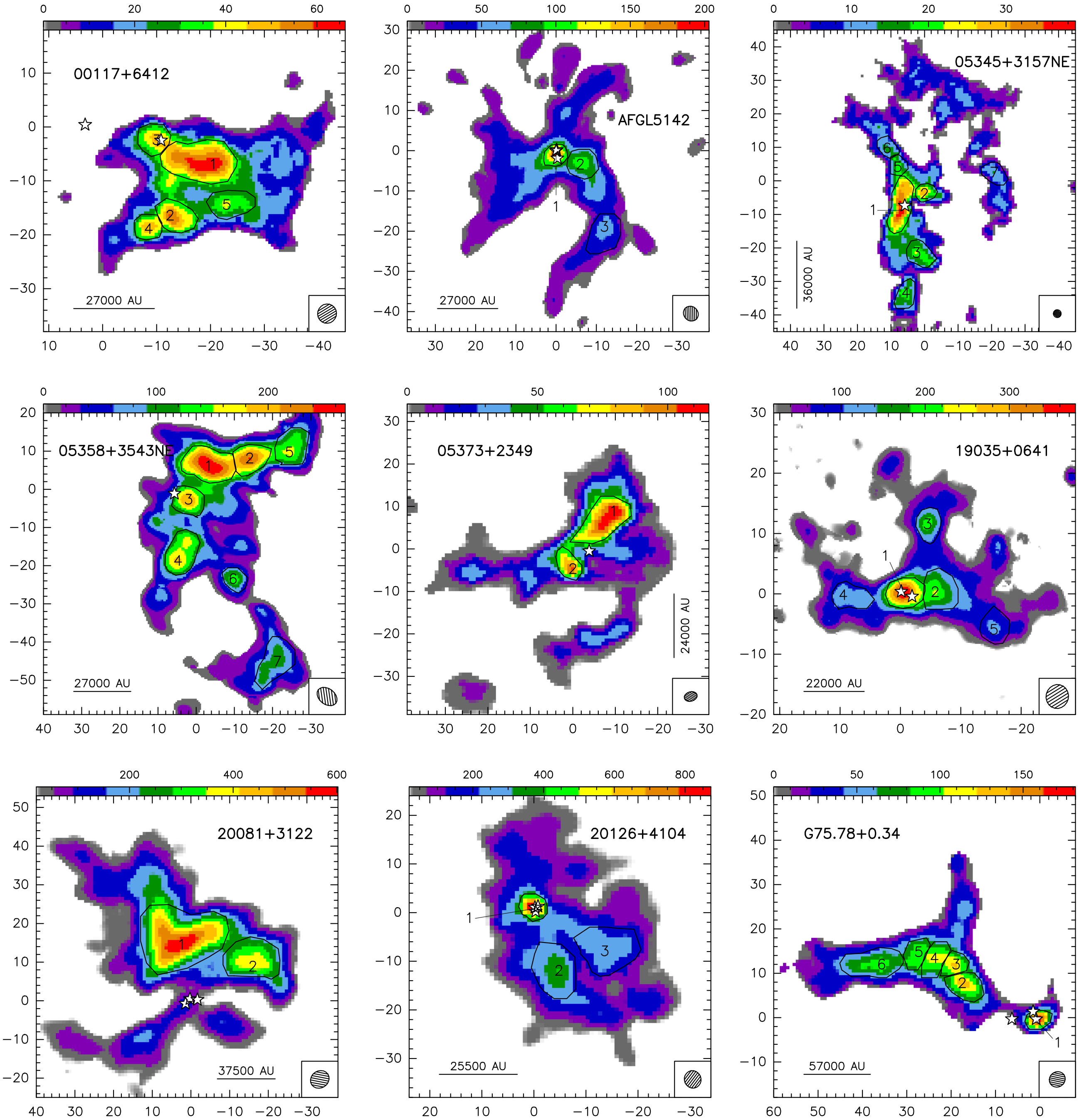

Figure 1. Colour image: NH_3 (1,1) zero-order moment (integrated intensity) maps in units of mJy km s^{-1} (horizontal colour-bar on the top of each panel). Coordinates in the x and y axis are right ascension and declination offsets in arcsec, with the (0,0) corresponding to the phase centre of the map (see Table 1). Black thick lines show the polygons for each core listed in Table 3, as obtained from the CLUMPFIND analysis (see Sect. 3). The numbers inside the polygons identify the core (see Table 3). The synthesised beams (listed in Table 1) are shown in the bottom-right corner of each panel. Star symbols in all panels correspond to centimetre continuum sources.

maps were constructed by integrating the emission of all the hyperfine components, while for the first and second-order moment maps we considered only the main hyperfine component, except for 20126+4104 for which the inner satellite hyperfine component was used (in the zeroth, first and second order moments) to avoid the high opacities in the main line. The integrated intensity maps reveal ammonia emission in all the regions, coming from compact condensations surrounded by faint and more extended emission. In the first-order moment maps (see Fig. B1), we identify large-scale velocity gradients (see e. g., AFGL 5142, 20081+3122, G75.78+0.34, 22172+5549N), not only associated with the compact condensations or cores but with the whole ammonia emission, probably revealing the large scale kinematics of the cloud. To extract and identify the cores within each region we ran the two-dimensional CLUMPFIND algorithm (Williams et al. 1994) on the NH_3 (1,1) zero-order moment map. This algorithm requires two input parameters:

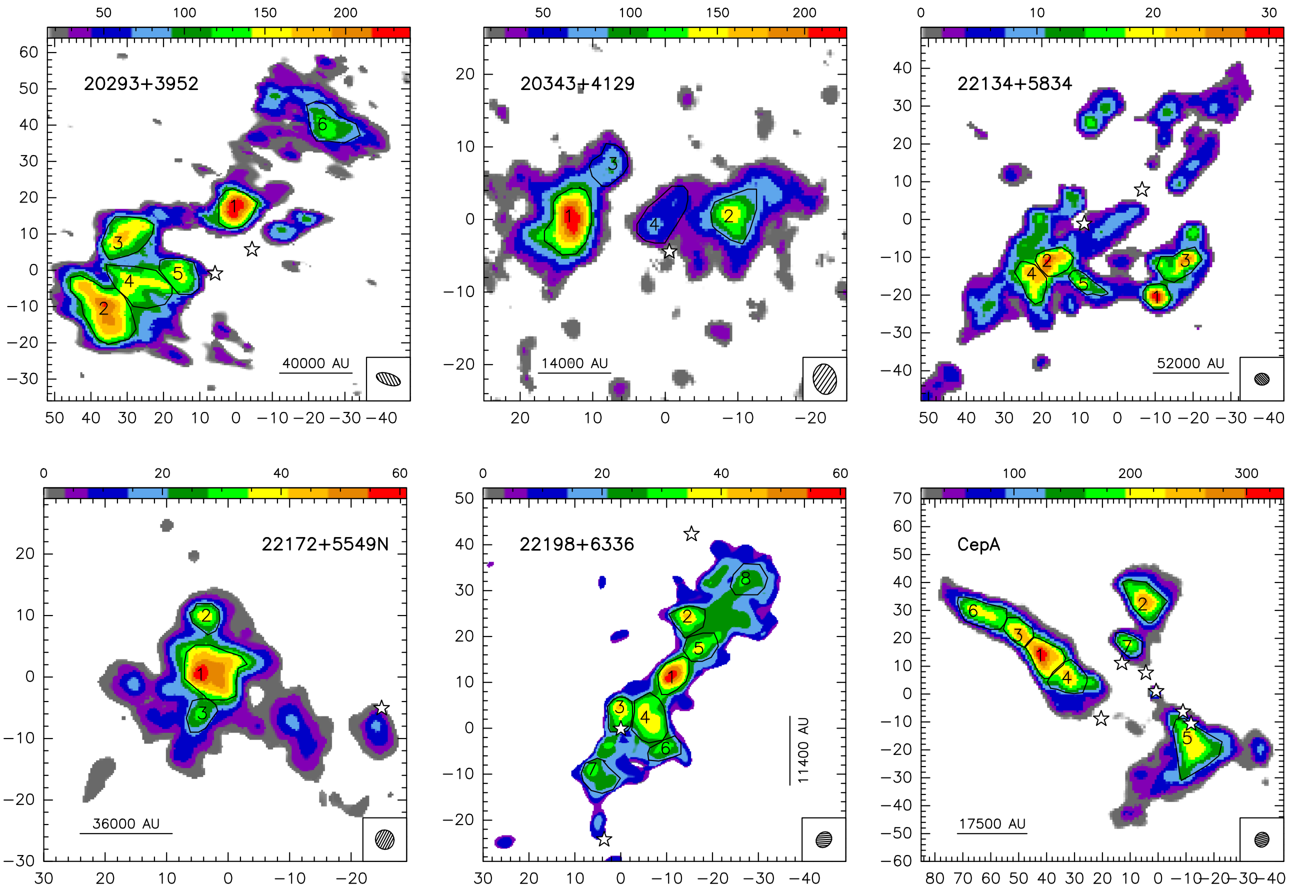

Figure 1 – *continued*

the 'bottom' level, corresponding to the lowest intensity to be included in the core, and the 'step', which determines the intensity increment required to differentiate one core from another core (see e. g., Miettinen et al. 2012 for further details). In our case, we used 'bottom' values of around 20–40% of the peak intensity of the zero-order moment, and 'steps' in the range 5–10% of the peak intensity (see last columns in Table 1). The output parameters defining each core returned by CLUMPFIND are the peak position, peak intensity and the flux density of the core. For each identified core we defined a polygon at the level of the full width at half maximum (FWHM; see black thick lines in Fig. 1). In Table 3 we list the offset position of each core (relative to the phase centre; listed in Table 1) and the deconvolved FWHM size. A total of 73 cores were identified.

The studied field of view (VLA primary beam at 1.3 cm) is $\sim$ 2 arcmin, or 1.5 pc at a distance of 2.5 kpc. On average, we found of the order of 5–6 cores in each region, with diametres $\sim$ 0.06 pc. We classify the identified cores as starless or protostellar (see Table 4), based on their infrared properties (from the *Spitzer*/IRAC, *Spitzer*/MIPS or WISE[2] images) and other observational evidence reported in the literature (e. g., molecular outflows, masers, HII regions, radiojets; see references in Table B1), summarized in Table B1. Within the starless cores we consider two groups: 'quiescent starless' and 'perturbed starless' cores. The former group includes cores appearing dark in the IRAC images, away ($\gtrsim 10''$) from strong IR sources or outflows, with or without millimetre continuum. On the other hand, perturbed starless cores are neither associated with a point infrared source but lie close ($\lesssim 10''$) to a bright IR source and/or along the axis of a molecular outflow, suggesting that these cores might be perturbed[3]. A core is classified as 'protostellar' if it is associated with an infrared point source, and with other star formation signposts (e. g., maser, outflow, centimetre continuum). Some cores were tentatively classified as 'protostellar?' if the only hint of star formation is the association with an infrared point source, which could be a background or foreground star not associated with the dense core. These tentatively classified cores are not included in our statistical analysis when comparing the different types of cores, to avoid contamination by misclassified cores. In Fig. 1, the stars indicate the position of centimetre continuum sources, likely tracing HII regions or thermal radio jets. In many cases, the most massive source of the region, usually associated with a strong centimetre source, tracing an (ultracompact) HII region is located offset of the core peaks (e. g., 20081+3122, 20293+3952, 20343+4129).

---

[2] The Wide-filed Infrared Survey Explorer (WISE) is described in (Wright et al. 2010).

[3] The differentiation between quiescent and perturbed starless cores was already introduced in Fontani et al. (2011).

Table 3. Physical parameters of the ammonia cores identified toward the 15 massive star-forming regions

			Offset[a]		Size[b]	NH_3 (1,1)[c]				NH_3 (2,2)[c]				
`ID`	Region	#	Δx	Δy	(pc)	$A \times \tau$	v	Δv	τ[d]	$T_{\rm mb}$	v	Δv	$T_{\rm rot}$[e]	$N_{\rm NH_3}$[e]
01	00117+6412	1	−20.5	−7.0	0.085	8.2 ± 1.0	−36.2 ± 0.1	0.8 ± 0.1	1.80 ± 0.29	1.4 ± 0.2	−36.1 ± 0.1	1.0 ± 0.2	14.6 ± 0.9	8.4 ± 0.9
02		2	−12.5	−16.5	0.046	4.5 ± 1.3	−35.5 ± 0.1	1.2 ± 0.2	1.40 ± 0.62	0.5 ± 0.2	−35.6 ± 0.6	2.4 ± 1.3	12.3 ± 1.5	10.1 ± 2.3
03		3	−10.0	−2.5	0.039	2.5 ± 0.3	−36.4 ± 0.1	1.6 ± 0.3	< 0.26	0.6 ± 0.2	−36.0 ± 0.5	2.2 ± 1.0	15.8 ± 0.8	2.9 ± 0.6
04		4	−8.5	−19.0	0.026	3.5 ± 1.4	−35.1 ± 0.2	1.4 ± 0.3	0.77 ± 0.82	0.8 ± 0.3	−35.0 ± 0.3	1.0 ± 0.6	15.4 ± 2.9	6.4 ± 2.0
05		5	−23.0	−14.5	0.048	8.1 ± 2.3	−36.3 ± 0.1	0.6 ± 0.1	3.45 ± 0.97	0.6 ± 0.3	−36.3 ± 0.3	0.8 ± 0.6	11.3 ± 1.8	13.2 ± 3.4
06	AFGL5142	1	+0.0	−1.0	0.040	12.3 ± 1.7	−2.2 ± 0.2	3.8 ± 0.2	1.35 ± 0.30	7.1 ± 0.6	−4.0 ± 0.2	4.6 ± 0.5	36.0 ± 3.9	41.1 ± 6.0
07		2	−6.0	−3.5	0.059	12.9 ± 1.5	−3.2 ± 0.1	1.7 ± 0.1	0.69 ± 0.25	9.2 ± 0.5	−3.8 ± 0.1	1.4 ± 0.1	32.5 ± 3.1	16.5 ± 2.3
08		3	−12.0	−19.0	0.073	9.2 ± 2.2	−5.0 ± 0.1	1.4 ± 0.2	1.19 ± 0.53	3.5 ± 0.2	−4.5 ± 0.1	1.6 ± 0.1	21.2 ± 3.5	12.4 ± 2.7
09	05345+3157NE	1	+6.4	−8.8	0.090	11.8 ± 0.6	−17.7 ± 0.1	1.3 ± 0.1	1.64 ± 0.13	2.3 ± 0.2	−17.7 ± 0.1	1.7 ± 0.1	15.3 ± 0.4	16.4 ± 0.9
10		2	+0.0	−4.0	0.046	10.8 ± 0.9	−18.3 ± 0.1	1.0 ± 0.1	1.06 ± 0.17	3.2 ± 0.3	−18.4 ± 0.1	0.9 ± 0.1	18.1 ± 0.8	9.0 ± 0.8
11		3	+2.4	−21.6	0.065	17.7 ± 1.1	−18.1 ± 0.1	0.5 ± 0.1	1.90 ± 0.16	2.9 ± 0.3	−18.0 ± 0.1	0.5 ± 0.1	14.5 ± 0.5	10.2 ± 0.7
12		4	+5.6	−33.6	0.059	8.8 ± 0.8	−17.1 ± 0.1	1.0 ± 0.1	1.27 ± 0.21	2.0 ± 0.2	−17.2 ± 0.1	1.1 ± 0.2	16.1 ± 0.8	10.8 ± 0.8
13		5	+8.0	+4.0	0.045	17.3 ± 1.4	−17.6 ± 0.1	0.5 ± 0.1	1.95 ± 0.19	2.3 ± 0.3	−17.6 ± 0.1	0.8 ± 0.1	13.2 ± 0.6	10.2 ± 0.9
14		6	+11.2	+9.6	0.047	17.4 ± 1.3	−17.9 ± 0.1	0.4 ± 0.1	2.53 ± 0.23	1.1 ± 0.4	−17.8 ± 0.1	0.6 ± 0.2	10.7 ± 0.4	12.0 ± 1.0
15		7	−20.8	+2.4	0.056	10.9 ± 1.1	−17.9 ± 0.1	0.4 ± 0.1	1.48 ± 0.23	2.5 ± 0.4	−17.9 ± 0.1	0.4 ± 0.1	16.3 ± 1.0	5.1 ± 0.5
16	05358+3543NE	1	−3.2	+6.0	0.089	9.5 ± 0.7	−34.6 ± 0.1	1.2 ± 0.1	< 0.14	5.7 ± 0.3	−34.5 ± 0.1	1.4 ± 0.1	23.4 ± 0.9	7.1 ± 0.8
17		2	−14.0	+8.0	0.061	14.5 ± 1.5	−35.4 ± 0.1	0.8 ± 0.1	1.14 ± 0.22	4.3 ± 0.4	−35.4 ± 0.1	1.3 ± 0.1	18.2 ± 1.1	9.9 ± 1.1
18		3	+2.0	−2.8	0.055	5.9 ± 0.3	−35.0 ± 0.1	1.7 ± 0.1	< 0.07	4.4 ± 0.4	−35.1 ± 0.1	1.8 ± 0.2	26.6 ± 1.0	6.2 ± 0.6
19		4	+4.8	−18.8	0.074	6.7 ± 1.2	−35.8 ± 0.1	1.3 ± 0.1	0.30 ± 0.36	3.8 ± 0.3	−35.7 ± 0.1	1.2 ± 0.1	23.9 ± 2.5	6.5 ± 1.2
20		5	−24.4	+9.6	0.069	16.5 ± 3.0	−36.1 ± 0.1	0.5 ± 0.1	2.26 ± 0.50	3.6 ± 0.7	−36.1 ± 0.1	0.7 ± 0.2	16.9 ± 2.2	9.5 ± 1.7
21		6	−9.6	−23.6	0.031	15.6 ± 2.6	−36.7 ± 0.1	0.5 ± 0.1	1.69 ± 0.38	2.1 ± 0.4	−36.8 ± 0.2	1.3 ± 0.3	13.2 ± 1.1	8.7 ± 1.4
22		7	−21.2	−45.2	0.078	7.6 ± 1.3	−37.3 ± 0.1	0.9 ± 0.1	1.10 ± 0.36	1.3 ± 0.4	−37.3 ± 0.2	1.1 ± 0.4	14.2 ± 1.1	12.9 ± 1.2
23	05373+2349	1	−9.6	+8.8	0.081	12.3 ± 0.5	+2.0 ± 0.1	1.0 ± 0.1	1.23 ± 0.13	3.4 ± 0.1	+2.1 ± 0.1	1.4 ± 0.1	17.8 ± 0.5	10.4 ± 0.6
24						18.3 ± 1.6	+3.2 ± 0.1	0.6 ± 0.1	3.15 ± 0.28	2.9 ± 0.1	+3.3 ± 0.1	0.7 ± 0.1	14.9 ± 1.0	13.2 ± 1.3
25		2	+0.0	−4.8	0.044	11.1 ± 0.6	+1.5 ± 0.1	1.2 ± 0.1	1.16 ± 0.16	3.4 ± 0.1	+2.1 ± 0.1	1.4 ± 0.1	18.7 ± 0.6	11.2 ± 0.6
26						9.7 ± 1.5	+2.6 ± 0.1	0.5 ± 0.1	0.57 ± 0.30	4.2 ± 0.2	+2.5 ± 0.1	0.5 ± 0.1	21.1 ± 1.9	3.4 ± 0.6
27	19035+0641	1	−0.5	+0.3	0.044	5.9 ± 1.1	+32.4 ± 0.2	4.4 ± 0.3	0.61 ± 0.36	3.3 ± 0.2	+33.0 ± 0.2	5.0 ± 0.4	25.0 ± 3.1	21.0 ± 3.8
28		2	−5.8	+0.3	0.050	4.7 ± 0.3	+32.9 ± 0.1	3.1 ± 0.2	< 0.15	3.4 ± 0.2	+33.1 ± 0.1	3.0 ± 0.2	26.0 ± 1.0	9.2 ± 0.9
29		3	−4.5	+11.5	0.028	5.1 ± 0.9	+34.2 ± 0.1	2.7 ± 0.2	0.30 ± 0.33	1.4 ± 0.3	+34.2 ± 0.3	2.3 ± 0.4	16.4 ± 1.2	11.7 ± 2.0
30		4	+9.5	−0.3	0.036	4.0 ± 0.8	+32.2 ± 0.2	2.8 ± 0.3	0.33 ± 0.43	1.3 ± 0.2	+32.3 ± 0.3	2.8 ± 0.5	17.9 ± 1.7	9.1 ± 1.8
31		5	−15.5	−6.0	0.034	6.4 ± 1.3	+31.9 ± 0.1	1.6 ± 0.2	1.52 ± 0.46	1.2 ± 0.3	+31.7 ± 0.2	1.3 ± 0.4	15.0 ± 1.7	13.2 ± 2.3
32	20081+3122	1	+1.6	+15.2	0.232	15.6 ± 1.7	+10.5 ± 0.1	2.1 ± 0.1	2.10 ± 0.28	4.0 ± 0.3	+10.4 ± 0.1	2.7 ± 0.2	18.2 ± 1.5	31.1 ± 3.4
33		2	−16.8	+9.6	0.140	7.6 ± 0.9	+11.9 ± 0.1	1.2 ± 0.1	0.89 ± 0.36	2.4 ± 0.2	+11.9 ± 0.1	1.4 ± 0.2	18.4 ± 1.2	8.7 ± 1.0
34						6.4 ± 0.9	+13.6 ± 0.1	1.3 ± 0.1	0.23 ± 0.30	3.0 ± 0.2	+13.5 ± 0.1	1.6 ± 0.2	20.9 ± 1.6	6.5 ± 1.0
35	20126+4104	1	+0.0	+0.8	0.033	21.9 ± 2.4	−4.3 ± 0.2	4.7 ± 0.2	2.09 ± 0.28	8.4 ± 0.6	−4.1 ± 0.2	5.5 ± 0.5	27.7 ± 2.5	81.5 ± 9.6
36		2	−4.8	−12.0	0.076	85.7 ± 5.0	−4.5 ± 0.1	0.8 ± 0.1	5.40 ± 0.34	11.8 ± 0.4	−4.5 ± 0.1	1.2 ± 0.1	15.7 ± 1.0	58.8 ± 5.0
37		3	−13.6	−8.0	0.084	52.0 ± 4.0	−4.5 ± 0.1	0.9 ± 0.1	3.89 ± 0.26	9.3 ± 0.3	−4.5 ± 0.1	1.2 ± 0.1	17.0 ± 1.3	39.3 ± 3.8
38	G75.78+0.34	1	+0.7	−0.7	0.062	5.1 ± 0.6	+0.2 ± 0.3	4.6 ± 0.6	< 0.22	5.6 ± 0.6	+0.4 ± 0.3	4.5 ± 0.6	35.2 ± 3.3	15.7 ± 2.8
39		2	+17.5	+7.7	0.113	5.2 ± 0.4	+0.4 ± 0.2	3.0 ± 0.3	< 0.11	3.6 ± 0.4	+0.4 ± 0.2	2.8 ± 0.3	25.4 ± 1.2	10.5 ± 1.2
40		3	+18.9	+11.9	0.077	6.3 ± 0.8	+1.1 ± 0.2	2.6 ± 0.4	< 0.27	4.2 ± 0.4	+0.9 ± 0.2	2.8 ± 0.3	25.1 ± 1.9	11.1 ± 1.9
41		4	+23.8	+13.3	0.102	5.6 ± 0.3	+1.5 ± 0.1	1.3 ± 0.2	0.22 ± 0.03	3.3 ± 0.3	+1.5 ± 0.2	1.7 ± 0.3	24.1 ± 0.7	5.8 ± 0.6
42						5.7 ± 0.7	−0.2 ± 0.1	1.3 ± 0.2	< 0.20	2.9 ± 0.3	−0.5 ± 0.2	1.8 ± 0.3	21.5 ± 1.3	5.4 ± 0.9
43		5	+27.3	+14.7	0.080	6.3 ± 0.9	+0.3 ± 0.1	2.4 ± 0.2	0.14 ± 0.37	3.2 ± 0.4	+0.3 ± 0.2	3.0 ± 0.4	21.8 ± 1.6	12.4 ± 1.7
44		6	+35.7	+11.9	0.162	8.6 ± 1.2	−0.2 ± 0.1	1.4 ± 0.1	0.17 ± 0.36	4.5 ± 0.4	−0.2 ± 0.1	1.3 ± 0.1	22.3 ± 1.8	10.8 ± 1.4

Table 3 – *continued*

		Offset[a]		Size[b]	NH_3 (1,1)[c]				NH_3 (2,2)[c]				
`ID` Region	#	Δx	Δy	(pc)	$A \times \tau$	v	Δv	τ[d]	$T_{\rm mb}$	v	Δv	$T_{\rm rot}$[e]	$N_{\rm NH_3}$[e]
45 20293+3952	1	+0.0	+18.0	0.089	16.7 ± 4.4	$+7.3 \pm 0.1$	1.1 ± 0.1	3.33 ± 0.88	3.0 ± 0.6	$+7.4 \pm 0.2$	1.3 ± 0.3	16.3 ± 3.6	20.4 ± 5.5
46	2	+36.0	−10.0	0.148	23.1 ± 3.9	$+6.0 \pm 0.1$	0.9 ± 0.1	4.84 ± 0.72	2.6 ± 0.3	$+6.1 \pm 0.1$	1.6 ± 0.2	13.4 ± 2.0	35.4 ± 5.8
47	3	+32.0	+8.0	0.112	6.4 ± 1.0	$+5.9 \pm 0.1$	2.1 ± 0.2	1.63 ± 0.37	2.0 ± 0.2	$+6.0 \pm 0.2$	2.9 ± 0.4	20.1 ± 2.2	18.7 ± 2.1
48	4	+29.0	−2.5	0.125	13.3 ± 2.3	$+5.5 \pm 0.1$	1.0 ± 0.1	2.87 ± 0.55	2.4 ± 0.3	$+5.6 \pm 0.1$	1.8 ± 0.2	15.6 ± 2.0	18.5 ± 2.8
49	5	+15.5	−0.5	0.083	12.8 ± 2.8	$+5.3 \pm 0.1$	1.0 ± 0.1	2.80 ± 0.63	2.7 ± 0.3	$+5.4 \pm 0.1$	1.6 ± 0.2	17.5 ± 3.2	15.0 ± 3.2
50	6	−24.5	+40.5	0.103	8.5 ± 1.8	$+4.9 \pm 0.1$	1.3 ± 0.1	2.18 ± 0.54	1.4 ± 0.2	$+4.9 \pm 0.2$	1.9 ± 0.3	14.8 ± 1.9	23.9 ± 2.8
51 20343+4129	1	+12.9	+0.8	0.044	11.6 ± 2.3	$+11.8 \pm 0.1$	1.9 ± 0.2	2.04 ± 0.52	2.6 ± 0.6	$+11.9 \pm 0.3$	2.5 ± 0.6	16.7 ± 2.3	23.9 ± 4.6
52	2	−9.1	−0.8	0.035	6.7 ± 0.9	$+10.9 \pm 0.1$	1.6 ± 0.3	< 0.24	2.5 ± 0.7	$+10.9 \pm 0.2$	0.9 ± 0.3	18.5 ± 1.2	7.1 ± 1.6
53	3	+6.8	+8.0	0.023	4.6 ± 1.1	$+13.0 \pm 0.2$	1.3 ± 0.4	< 0.25	2.2 ± 1.7	$+12.4 \pm 0.4$	0.4 ± 0.3	20.8 ± 2.5	3.8 ± 1.5
54	4	+1.1	−0.4	0.036	6.1 ± 2.0	$+10.2 \pm 0.1$	1.1 ± 0.2	0.60 ± 0.67	2.1 ± 0.5	$+10.2 \pm 0.2$	1.0 ± 0.3	18.8 ± 3.3	5.3 ± 1.8
55 22134+5834	1	−10.4	−20.7	0.071	9.7 ± 1.8	-19.2 ± 0.1	0.7 ± 0.1	3.15 ± 0.57	1.2 ± 0.2	-19.2 ± 0.1	0.8 ± 0.2	13.1 ± 1.6	12.2 ± 2.1
56	2	+18.6	−11.0	0.094	5.1 ± 0.5	-18.7 ± 0.1	1.0 ± 0.1	1.21 ± 0.22	2.1 ± 0.2	-18.7 ± 0.1	1.0 ± 0.1	22.7 ± 1.7	5.7 ± 0.5
57	3	−17.9	−11.0	0.107	7.4 ± 0.6	-18.7 ± 0.1	0.6 ± 0.1	1.94 ± 0.22	1.1 ± 0.2	-18.7 ± 0.1	0.8 ± 0.2	13.9 ± 0.7	7.1 ± 0.6
58	4	+22.8	−14.5	0.100	3.2 ± 0.6	-18.4 ± 0.1	1.2 ± 0.1	0.49 ± 0.35	1.0 ± 0.1	-18.4 ± 0.1	1.2 ± 0.2	17.3 ± 1.6	4.1 ± 0.6
59	5	+9.0	−17.3	0.068	3.5 ± 0.7	-18.7 ± 0.1	0.9 ± 0.1	0.92 ± 0.41	1.2 ± 0.2	-18.9 ± 0.1	1.0 ± 0.2	19.7 ± 2.3	3.6 ± 0.5
60 22172+5549N	1	+4.5	+0.3	0.099	4.2 ± 0.6	-43.2 ± 0.1	1.4 ± 0.1	0.25 ± 0.26	1.8 ± 0.2	-43.3 ± 0.1	1.5 ± 0.2	20.3 ± 1.4	4.5 ± 0.6
61	2	+3.6	+9.9	0.040	5.6 ± 1.5	-43.9 ± 0.1	0.9 ± 0.1	1.06 ± 0.57	1.3 ± 1.7	-44.0 ± 2.0	0.8 ± 3.0	16.0 ± 2.2	5.3 ± 1.3
62	3	+4.2	−6.0	0.039	3.2 ± 0.8	-43.6 ± 0.1	1.8 ± 0.2	1.31 ± 0.54	0.9 ± 0.6	-43.5 ± 1.0	2.3 ± 1.0	17.5 ± 2.6	8.2 ± 1.5
63 22198+6336	1	−11.0	+11.0	0.023	11.2 ± 2.2	-10.6 ± 0.1	1.0 ± 0.1	1.38 ± 0.43	1.5 ± 0.6	-10.7 ± 0.2	1.0 ± 0.5	13.2 ± 1.2	12.9 ± 2.5
64	2	−14.5	+24.3	0.021	7.2 ± 1.9	-10.8 ± 0.1	0.9 ± 0.1	0.83 ± 0.50	1.9 ± 0.9	-10.8 ± 0.1	0.5 ± 0.2	16.6 ± 2.1	7.3 ± 1.6
65	3	+0.3	+4.5	0.021	6.4 ± 1.4	-10.5 ± 0.1	1.1 ± 0.1	0.60 ± 0.40	2.4 ± 0.4	-10.7 ± 0.2	1.4 ± 0.3	19.4 ± 2.2	5.9 ± 1.2
66	4	−5.3	+2.3	0.031	9.2 ± 1.4	-10.6 ± 0.1	0.9 ± 0.1	1.56 ± 0.33	1.5 ± 0.3	-10.7 ± 0.2	1.9 ± 0.5	14.1 ± 1.1	10.2 ± 1.4
67	5	−17.0	+17.3	0.020	16.1 ± 3.6	-10.8 ± 0.1	0.5 ± 0.1	2.33 ± 0.62	2.4 ± 1.2	-10.7 ± 0.2	0.4 ± 0.2	14.1 ± 1.9	9.0 ± 2.1
68	6	−9.8	−4.5	0.017	3.8 ± 0.5	-10.9 ± 0.1	1.2 ± 0.2	< 0.29	1.6 ± 0.6	-11.1 ± 0.2	0.9 ± 0.5	19.4 ± 1.2	3.2 ± 0.7
69	7	+6.3	−9.0	0.024	11.5 ± 2.9	-11.5 ± 0.1	0.6 ± 0.1	2.52 ± 0.70	2.5 ± 0.6	-11.4 ± 0.1	0.8 ± 0.3	17.1 ± 3.3	8.2 ± 2.1
70	8	−27.3	+32.5	0.023	16.3 ± 3.9	-11.5 ± 0.1	0.3 ± 0.1	2.93 ± 0.73	...	...	...		
71 CepA	1	+41.6	+14.4	0.039	8.9 ± 1.0	-11.7 ± 0.1	1.3 ± 0.1	0.54 ± 0.24	4.1 ± 0.3	-11.6 ± 0.1	1.5 ± 0.1	21.9 ± 1.5	13.4 ± 1.1
72	2	+4.8	+32.8	0.041	22.4 ± 2.1	-10.2 ± 0.1	0.5 ± 0.1	2.13 ± 0.26	5.7 ± 0.5	-10.2 ± 0.1	0.8 ± 0.1	18.3 ± 1.3	11.5 ± 1.0
73	3	+49.6	+21.6	0.027	7.4 ± 1.4	-11.9 ± 0.1	1.5 ± 0.1	0.39 ± 0.32	3.1 ± 0.3	-12.0 ± 0.1	1.9 ± 0.2	20.2 ± 2.0	15.3 ± 1.6
74	4	+32.0	+6.4	0.036	9.7 ± 0.8	-12.0 ± 0.1	0.9 ± 0.1	0.48 ± 0.18	5.2 ± 0.3	-12.0 ± 0.1	1.0 ± 0.1	23.8 ± 1.3	7.7 ± 0.6
75	5	−11.2	−15.2	0.056	10.4 ± 1.6	-9.5 ± 0.1	0.8 ± 0.1	0.49 ± 0.27	6.3 ± 0.3	-9.5 ± 0.1	0.9 ± 0.1	26.0 ± 2.8	6.1 ± 1.0
76	6	+65.6	+30.4	0.041	13.7 ± 1.5	-12.1 ± 0.1	0.7 ± 0.1	2.17 ± 0.30	3.2 ± 0.2	-12.1 ± 0.1	1.0 ± 0.1	17.5 ± 1.4	31.1 ± 1.2
77	7	+10.4	+17.6	0.023	17.8 ± 2.4	-10.8 ± 0.1	0.5 ± 0.1	2.33 ± 0.34	5.1 ± 0.6	-10.8 ± 0.1	0.7 ± 0.1	20.6 ± 2.3	8.0 ± 1.1

[a] Offset (in arcsec) between the position of the core and the phase centre (see Table 2). x and y correspond to right ascension and declination, respectively.

[b] Linear diametre of the clump computed from the deconvolved angular diametre, $\theta_{\rm S}$, which has been calculated assuming the cores are Gaussians from the expression $\theta_{\rm S}^2 = {\rm FWHM}^2 - {\rm HPBW}^2$, with ${\rm FWHM} = 2\sqrt{A/\pi}$ and A being the area inside the polygons (shown in Fig. 1) and with HPBW corresponding to the geometric mean of the minor and major axes of the synthesised beams (see Table 2).

[c] Parameters obtained from the spectral fit to the NH_3 (1,1) and (2,2) lines: v and Δv are the velocity of the local standard of rest and the linewidth in km s^{-1}, and $T_{\rm mb}$ is the temperature of the line in K. The hyperfine structure of the (1,1) transition allows us to measure the opacity τ of the main line. The parameter $A \times \tau$ is defined as $A = f\,[J_\nu(T_{\rm ex}) - J_\nu(T_{\rm bg})]$ with $f = 1$ (see Appendix A).

[d] For a few cases, corresponding to the cores with optically thin emission, we provide an upper limit in the opacity. Even if τ cannot be determined with high precision, the derived quantities, $T_{\rm rot}$ and $N_{\rm NH_3}$, in the optically thin limit, depend on the line intensity, $A \times \tau$, which is very well constrained by the data (see Appendix A).

[e] Rotational temperature (in K) and column density (in 10^{14} cm^{-2}).

3.2 Averaged physical parameters for ammonia dense cores

For each core, we extracted the spectra averaged over the area assigned by the polygons (shown in Fig. 1) in both NH_3 (1,1) and (2,2) lines, and fitted the hyperfine structure of the NH_3 (1,1) transition following the procedure described in Appendix A, and a Gaussian to the NH_3 (2,2) line (see observed and fitted spectra in Fig. B2). This allowed us to obtain the opacity, velocity, and linewidth for each core[4]. We derived the rotational temperature and primary beam corrected ammonia column density following the procedure outlined in the appendix of Busquet et al. (2009). All these parameters are listed in Table 3. The average values of linewidth, opacity of the NH_3 (1,1) main line, rotational temperature, and ammonia column density of all the 73 cores are $\sim$ 1.4 km s^{-1}, 1.4, 19 K, and 10^{15} cm^{-2}, respectively. Our values of linewidth, rotational temperature and ammonia column density are very similar to the values obtained by Urquhart et al. (2011) for the RMS (Red MSX Source) survey, of 2 km s^{-1}, 22 K and 2×10^{15} cm^{-2}, even using very different observing techniques and sampling different spatial scales (single-dish vs interferometry). If we analyse the distributions of linewidth, opacity, rotational temperature, and column density for the starless and protostellar populations separately (see Fig. 2 panels A to E), the average values that we obtain are (i) $\sim$ 1.0 km s^{-1}, 1.5, 16.0 K, and 10^{15} cm^{-2} for quiescent starless cores, (ii) $\sim$ 1.4 km s^{-1}, 1.2, 19.3 K, and 10^{15} cm^{-2} for perturbed starless cores, and (iii) $\sim$ 1.8 km s^{-1}, 1.2, 21.3 K, and 10^{15} cm^{-2} for protostellar cores. Thus, quiescent starless cores have, as expected, linewidths and rotational temperatures smaller than protostellar cores (see Fig. 2 panels A and D; Table 5). The linewidths and temperatures of perturbed starless cores are in between the values measured for quiescent starless and protostellar cores, consistent with the fact that these cores were originally quiescent and then perturbed by the passage of outflows or the high radiation of a nearby bright infrared source. These cores might be similar to the 'warm' starless cores reported in Motte et al. (2010) using *Herschel* observations towards Cygnus X, and for some of them a low deuterium fractionation is measured (Fontani et al. 2011). Further studies should be carried out to assess the true nature of these perturbed starless cores.

The average values derived for the rotational temperature of quiescent starless and protostellar cores (of 16.0 K and 21.3 K, respectively, corresponding to kinetic temperatures of 18.8 K and 28.8 K, following Tafalla et al. 2004) can be compared to the values reported in the literature, although derived from observations of lower angular resolution. Olmi et al. (2013) studied the dense clumps in the Galactic field $l = 59^\circ$ (at a distance of 3.6 kpc, similar to the distances of our regions) within the Hi-GAL *Herschel* project (Molinari et al. 2010), and derived kinetic temperatures of 17 K for starless cores and 20 K for protostellar cores, following the same trend as we found in our cores. Urquhart et al. (2011) estimated the kinetic temperatures for clumps associated with young stellar objects and HII regions in the RMS survey to be in the range 20–25 K, also in agreement with our protostellar temperatures. However, it is worth noting that the average rotational temperature of 16 K found in the quiescent starless cores of our clustered massive star-forming regions is significantly larger than the values measured in starless cores of low-mass isolated regions (of about 10 K or even less; e. g., Tafalla et al. 2002, 2004; Rathborne et al. 2008; Rosolowsky et al. 2008; Schnee et al. 2010), and of infrared dark clouds with no active star formation ($\sim$ 10 K; e. g., Ragan et al. 2011). Temperatures of $\sim$ 15 K for starless cores are also found by Li et al. (2003) in the quiescent cores near the Trapezium cluster. Li et al. find that the temperatures of the massive quiescent cores can be well explained by the dust being heated by the external UV field from the Trapezium cluster, at a distance of $\sim$ 1 pc from the massive cores. This possibility is investigated for the regions in our sample in Sect. 4.1.

The linewidths measured in our starless cores have an important non-thermal component, which is almost negligible in low-mass clustered regions (e. g., Friesen et al. 2009; Foster et al. 2009). To evaluate this component, we assumed the relation $\sigma_{\rm nth} = \sqrt{\sigma_{\rm obs}^2 - \sigma_{\rm th}^2}$ where $\sigma_{\rm obs}$ is the measured velocity dispersion of the core ($= \Delta v/(8 \ln 2)^{1/2}$ for a Gaussian line profile with Δv the measured FWHM of the line) and $\sigma_{\rm th}$ is the thermal velocity dispersion. For NH_3, assuming a Maxwellian velocity distribution, $\sigma_{\rm th}$ can be calculated from $\sqrt{k_{\rm B}\, T_{\rm kin}/(\mu\, m_{\rm H})}$, with $k_{\rm B}$ the Boltzmann constant, μ the molecular weight (= 17.03 for ammonia), $m_{\rm H}$ the mass of the Hydrogen atom, and $T_{\rm kin}$ the kinetic temperature listed in Col. 3 of Table 4. In Cols. 5 and 6 of the same Table we list the non-thermal velocity dispersion ($\sigma_{\rm nth}$) and the non-thermal velocity dispersion over the isothermal sound speed ($\sigma_{\rm nth}/c_s$), where c_s is calculated using a mean molecular weight $\mu = 2.33$. From the distributions shown in Fig. 2 (panels H and I) we see that protostellar cores have a non-thermal component (0.76 km s^{-1}, or equivalently $\Delta v_{\rm nth}$ = 1.8 km s^{-1}) higher than the non-thermal component of the quiescent starless (0.44 km s^{-1}, or $\Delta v_{\rm nth}$ = 1.0 kms) and perturbed starless (0.56 km s^{-1}, or $\Delta v_{\rm nth}$ = 1.3 km s^{-1}) cores. For the $\sigma_{\rm nth}/c_s$ we obtain mean ratios of 1.7, 1.9 and 2.2 for quiescent starless, perturbed starless and protostellar cores, respectively (see Table 5), indicating that the cores are characterised by moderately supersonic non-thermal motions. In general our cores (both starless and protostellar), associated with intermediate and high-mass star-forming regions, have values of turbulent Mach number $\sim$ 2, being greater than those found in Perseus or Ophiucus (with values between 0.5 and 1.5; e. g., André et al. 2007; Friesen et al. 2009; Foster et al. 2009).

From the ammonia column density (listed in Table 3), we derived the mass of the core and the core mass surface density, following the procedures explained in the footnotes of Table 4. These two quantities are listed in Cols. 8 and 9 of Table 4, and their distributions are shown in panels F and G of Fig. 2. Starless and protostellar cores show similar mean masses ($\sim$ 1.0–1.8 $M_\odot$) and mean surface densities ($\sim$ 0.10–0.12 g cm^{-2}) (see Table 5).

3.3 Ammonia correlations

As presented in Sect. 3.2, we note some differences in the parameters derived for the starless and protostellar cores. In

---

[4] For four cores it was necessary to fit the ammonia spectra with two different velocity components (see Table 3 and Fig. B2).

Table 4. Derived parameters for the ammonia cores

`ID`	Type[a]	T_{kin}[b] (K)	σ_{th}[c] (km s^{-1})	σ_{nth}[c] (km s^{-1})	$\sigma_{\mathrm{nth}}/c_s$	σ_{tot} (km s^{-1})	M_{core}[d] ($M_{\odot}$)	Σ_{core}[e] (g cm^{-2})	M_{vir}[f] ($M_{\odot}$)
01	P	16.4	0.09	0.32	1.32	0.40	2.56	0.09	5.42
02	S	13.3	0.08	0.51	2.36	0.56	0.90	0.11	7.19
03	P	18.1	0.09	0.67	2.63	0.71	0.18	0.03	10.26
04	S*	17.5	0.09	0.60	2.41	0.65	0.18	0.07	5.59
05	P?	12.1	0.08	0.26	1.25	0.33	1.28	0.15	2.03
06	P	66.3	0.18	1.59	3.27	1.66	2.76	0.46	59.31
07	P?	53.9	0.16	0.71	1.61	0.83	2.41	0.18	17.99
08	P?	26.9	0.11	0.60	1.94	0.67	2.78	0.14	15.76
09	P	17.4	0.09	0.56	2.27	0.62	5.57	0.18	17.10
10	P	21.6	0.10	0.41	1.47	0.49	0.80	0.10	4.69
11	S	16.2	0.09	0.21	0.87	0.32	1.81	0.11	1.93
12	S	18.5	0.09	0.40	1.56	0.47	1.58	0.12	5.80
13	S	14.5	0.08	0.21	0.92	0.31	0.86	0.11	1.32
14	S	11.3	0.07	0.17	0.83	0.26	1.11	0.13	0.90
15	S	18.9	0.10	0.16	0.63	0.31	0.67	0.06	1.16
16	P	31.1	0.12	0.49	1.48	0.59	2.36	0.08	13.23
17	P?	21.8	0.10	0.33	1.18	0.43	1.54	0.11	4.20
18	P	38.0	0.14	0.69	1.89	0.78	0.79	0.07	16.01
19	S*	32.1	0.12	0.54	1.60	0.64	1.50	0.07	13.19
20	P	19.7	0.10	0.20	0.77	0.33	1.90	0.11	2.05
21	S*	14.6	0.08	0.17	0.76	0.28	0.35	0.10	0.66
22	S	15.9	0.09	0.37	1.55	0.44	3.28	0.14	6.49
23	P	21.1	0.10	0.40	1.45	0.48	2.87	0.12	7.92
24	P	16.8	0.09	0.25	1.04	0.35	3.62	0.15	3.42
25	S*	22.5	0.10	0.49	1.75	0.57	0.91	0.13	6.54
26	S*	26.6	0.11	0.17	0.56	0.35	0.28	0.04	1.10
27	P	34.4	0.13	1.87	5.37	1.91	1.70	0.23	90.38
28	S*	36.6	0.13	1.30	3.62	1.35	0.97	0.10	49.97
29	S	18.9	0.10	1.16	4.48	1.19	0.38	0.13	22.09
30	S*	21.3	0.10	1.17	4.24	1.20	0.49	0.10	28.71
31	S	16.9	0.09	0.67	2.72	0.71	0.64	0.15	8.92
32	P?	21.8	0.10	0.89	3.21	0.93	70.21	0.35	108.66
33	S	22.0	0.10	0.51	1.83	0.58	7.19	0.10	22.24
34	S	26.2	0.11	0.56	1.84	0.64	5.31	0.07	26.71
35	P	40.5	0.14	1.98	5.23	2.01	3.72	0.91	75.60
36	S	17.9	0.09	0.32	1.28	0.41	14.24	0.66	4.96
37	P?	19.8	0.10	0.36	1.35	0.45	11.64	0.44	6.77
38	P	63.2	0.18	1.93	4.07	1.98	2.54	0.18	135.01
39	S*	35.3	0.13	1.28	3.62	1.33	5.61	0.12	109.15
40	P?	34.5	0.13	1.09	3.12	1.15	2.76	0.12	54.11
41	S	32.5	0.13	0.55	1.61	0.64	2.55	0.07	18.66
42	S	27.4	0.12	0.54	1.72	0.62	2.35	0.06	17.82
43	S	27.9	0.12	1.03	3.26	1.07	3.33	0.14	49.72
44	P?	29.0	0.12	0.58	1.82	0.66	11.88	0.12	33.29
45	S*	18.9	0.10	0.44	1.71	0.51	6.78	0.23	10.54
46	S*	14.8	0.08	0.36	1.57	0.43	32.56	0.40	11.82
47	P	24.9	0.11	0.90	3.02	0.94	9.81	0.21	53.15
48	P?	17.8	0.09	0.42	1.68	0.49	12.15	0.21	13.55
49	P	20.6	0.10	0.43	1.59	0.51	4.33	0.17	9.43
50	P?	16.6	0.09	0.56	2.29	0.61	10.63	0.27	18.96
51	S*	19.4	0.10	0.82	3.14	0.86	1.94	0.27	17.51
52	S*	22.1	0.10	0.66	2.37	0.72	0.36	0.08	9.21
53	P?	26.1	0.11	0.54	1.77	0.62	0.08	0.04	4.03
54	P	22.7	0.10	0.43	1.53	0.52	0.29	0.06	4.18
55	S	14.3	0.08	0.29	1.28	0.37	2.59	0.14	3.75
56	S*	29.7	0.12	0.40	1.24	0.52	2.11	0.06	9.62
57	S	15.4	0.09	0.26	1.11	0.35	3.41	0.08	4.67
58	S	20.4	0.10	0.48	1.79	0.55	1.73	0.05	14.06
59	P?	24.3	0.11	0.35	1.21	0.46	0.70	0.04	5.42

Table 4 – *continued*

ID	Type[a]	$T_{\rm kin}$[b] (K)	$\sigma_{\rm th}$[c] (km s^{-1})	$\sigma_{\rm nth}$[c] (km s^{-1})	$\sigma_{\rm nth}/c_s$	$\sigma_{\rm tot}$ (km s^{-1})	$M_{\rm core}$[d] ($M_\odot$)	$\Sigma_{\rm core}$[e] (g cm^{-2})	$M_{\rm vir}$[f] ($M_\odot$)
60	P	25.2	0.11	0.60	2.00	0.67	1.85	0.05	21.32
61	S	18.3	0.09	0.36	1.39	0.44	0.36	0.06	3.15
62	P?	20.6	0.10	0.74	2.75	0.79	0.52	0.09	12.75
63	S	14.5	0.08	0.41	1.80	0.47	0.29	0.14	2.32
64	P?	19.3	0.10	0.39	1.49	0.47	0.14	0.08	1.97
65	P	23.7	0.11	0.46	1.60	0.55	0.11	0.07	2.76
66	S*	15.7	0.09	0.39	1.67	0.46	0.41	0.11	2.92
67	S	15.7	0.09	0.17	0.73	0.29	0.15	0.10	0.43
68	S	23.6	0.11	0.52	1.79	0.59	0.04	0.04	2.78
69	S	20.1	0.10	0.26	0.96	0.37	0.20	0.09	1.05
71	S*	28.2	0.12	0.55	1.75	0.64	0.85	0.15	7.25
72	S*	22.0	0.10	0.18	0.65	0.33	0.81	0.13	1.04
73	S*	25.1	0.11	0.61	2.06	0.68	0.47	0.17	6.11
74	P?	31.9	0.12	0.36	1.07	0.49	0.42	0.09	3.05
75	S*	36.6	0.13	0.30	0.85	0.47	0.81	0.07	3.60
76	S*	20.7	0.10	0.29	1.07	0.40	2.19	0.35	2.25
77	P	25.7	0.11	0.17	0.57	0.35	0.18	0.09	0.56

[a] Type of the core: S: quiescent starless, S*: perturbed starless, P: protostellar, and P?: possible protostellar (see Sect. 3.1 and Table B1).

[b] Kinetic temperature, in K, derived from the rotational temperature and following Tafalla et al. (2004). We emphasise that Tafalla et al. empirical relation is accurate only for temperatures $\lesssim 20$ K, and thus the kinetic temperature given here should be regarded, for high temperatures, as an approximation.

[c] Thermal ($\sigma_{\rm th}$) and non-thermal ($\sigma_{\rm nth}$) velocity dispersion, in km s^{-1}.

[d] Mass of the core derived as $M_{\rm core} = (N/X)\mu\, m_{\rm H} A$, with μ (= 2.8) the mean molecular mass per H molecule, A ($= \pi({\rm size}/2)^2$) the area, and assuming an abundance of NH_3 with respect to H_2 (X) for all the cores of 4.2×10^{-8} (e. g., Pillai et al. 2006; Foster et al. 2009; Friesen et al. 2009; Rygl et al. 2010; Chira et al. 2013).

[e] Core mass surface density derived as $\Sigma_{\rm core} = M_{\rm core}/A$.

[f] Virial mass derived from $M_{\rm vir} = 210\,[R/{\rm pc}]\,[\Delta v/{\rm km\ s^{-1}}]^2\ M_\odot$ assuming uniform density across the core (MacLaren et al. 1988; Estalella et al. 1993). R is the radius of the core (obtained from the diametre size listed in Table 3), and Δv is the intrinsic linewidth of the NH_3 (1,1) line (listed in Table 3).

Table 5. Mean values derived from the NH_3 observations (from Tables 3 and 4)

Core type	$T_{\rm rot}$ (K)	$T_{\rm kin}$ (K)	size (pc)	τ	$N_{\rm NH_3}$ (cm^{-2})	$M_{\rm core}$ ($M_\odot$)	$\Sigma_{\rm core}$ (g cm^{-2})	$\Delta V_{(1,1)}$ (km s^{-1})	$\sigma_{\rm nth}$ (km s^{-1})	$\sigma_{\rm nth}/c_s$	$M_{\rm vir}$ ($M_\odot$)
Quiescent starless	16.0	18.8	0.063	1.5	$10^{15.0}$	1.15	0.10	1.03	0.44	1.67	5.1
Perturbed starless	19.3	24.2	0.056	1.2	$10^{15.0}$	1.09	0.12	1.36	0.56	1.93	7.0
Protostellar	21.3	28.8	0.063	1.2	$10^{15.0}$	1.47	0.12	1.81	0.76	2.24	11.7
All sample	18.8	23.8	0.065	1.4	$10^{15.0}$	1.36	0.12	1.36	0.57	1.91	7.8

particular, an increase of the temperature and linewidth as we move toward more evolved objets (protostellar cores). In a search for a physical relation between the derived parameters, we plotted several quantities against others, shown as six scatter plots in Fig. 3. In these plots we show the distribution of starless and protostellar core samples in red-circles and blue-stars, respectively. We performed some statistical tests to search for possible correlations between the physical quantities. In the top right corner of each plot, we give Kendall's τ rank correlation coefficient and the Pearson correlation coefficient (ρ) to a least-squares fit (dotted lines). We find that in five of the six plots there is a possible correlation, with τ coefficients ~ 0.3, and ρ in the range 0.4–0.6.

In the top panels of Fig. 3, we show the relation between the temperature, the linewidth and the mass of the core with the bolometric luminosity of the region, while in the bottom panels, we compare the temperature, the ammonia column density and the size of the core with the observed linewidth. We note that we are not able to derive a bolometric luminosity for each individual ammonia core but a single luminosity of the whole region[5]. Thus, the plots in Fig. 3 must be interpreted as a correlation between the properties of the cores within a region with respect to the luminosity of the region (which is in general dominated by the brightest mid-IR source). We find a correlation in five of the six panels (panels A to E of Fig. 3). Similar trends between the same parame-

---

[5] To estimate the bolometric luminosity $L_{\rm bol}$ (listed in Table 1), we compiled the flux densities at different frequencies from 2MASS, *Spitzer*/IRAC+MIPS, WISE, MSX, IRAS and JCMT (SCUBA; Di Francesco et al. 2008) catalogues and followed the methodology explained in Palau et al. (2013).

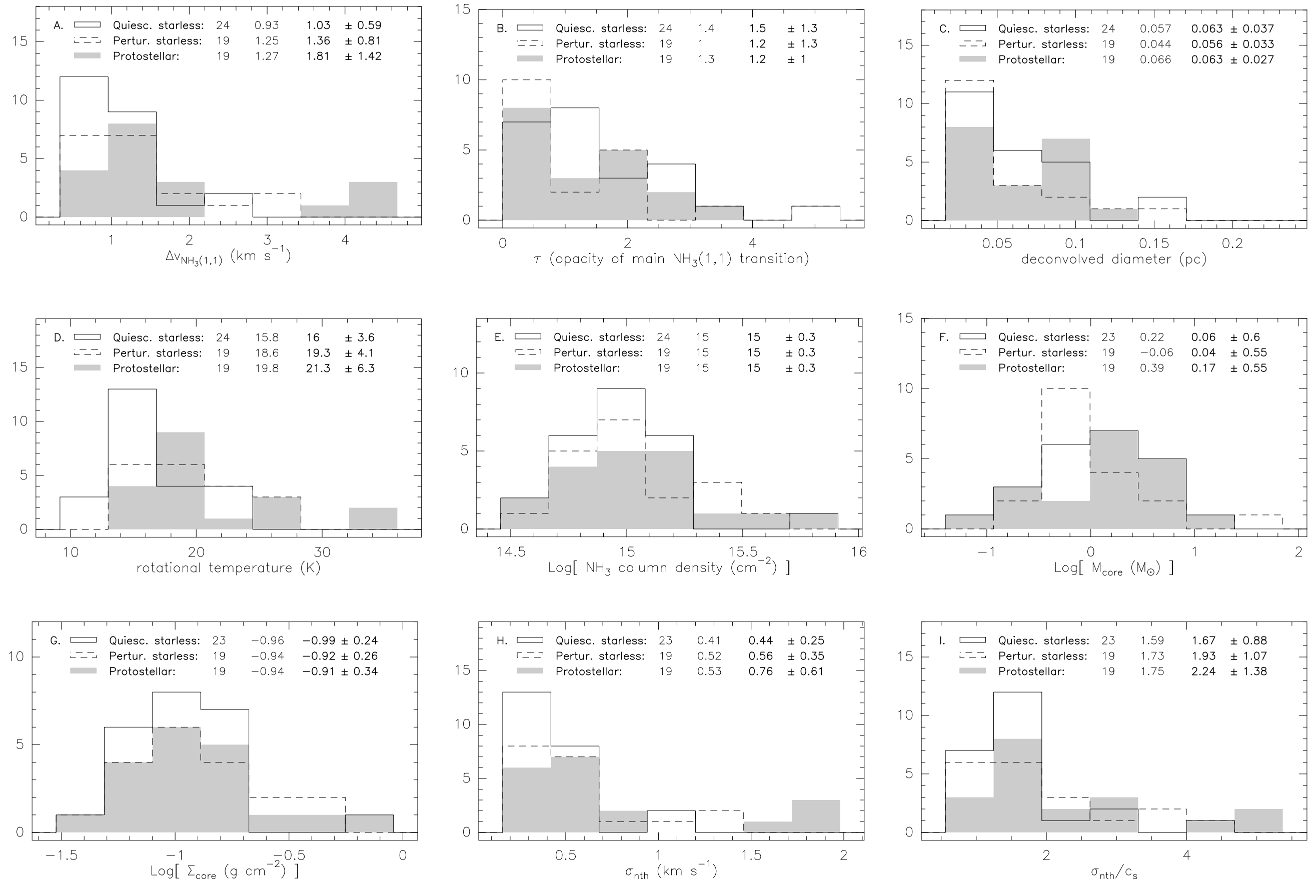

Figure 2. Distributions of: **(a)** NH_3 (1,1) linewidth, **(b)** opacity, **(c)** deconvolved diametre, **(d)** rotational temperature, **(e)** ammonia column density, **(f)** core mass $M_{\rm core}$, **(g)** core surface density $\Sigma_{\rm core}$, **(h)** non-thermal dispersion $\sigma_{\rm nth}$, and **(i)** non-thermal to thermal velocity dispersion ratio $\sigma_{\rm nth}/c_s$, for quiescent starless (solid line histrogram), perturbed starless (dashed line histogram), and protostellar (grey filled histogram) cores. The numbers at the top of each panel are the total number of sources used in the histogram, the median, and the mean ± standard deviation values.

ters have been reported from single-dish observational studies (e. g., Churchwell et al. 1990; Myers et al. 1991; Jijina et al. 1999; Rygl et al. 2010; Urquhart et al. 2011; Sepúlveda et al. 2011). Our correlations found in ammonia at higher angular resolution thus confirm that these relations take place also at the smaller spatial scales (~ 0.05 pc) of individual cores, and are not an observational (average) artifact due to the poor angular resolution of single-dish observations when studying clumps of sizes $\sim$ 0.1–10 pc. It is worth noting that in panel B (linewidth vs luminosity) there are four cores with linewidths ~ 4 km s^{-1}, located well above the trend found for the other cores. These four cores (AFGL 5142–1; 19035+0641–1; 20126+4104–1; G75.78+0.34–1) are known to be associated with powerful outflows that could perturb the motions of the dense gas close to the powering source (see Zhang et al. 2002; Cesaroni et al. 2005; Sánchez-Monge 2011; Sánchez-Monge et al. 2013). Finally, in panel F, we investigate a possible relation between the size of the core and its linewidth. Since the publication of the Larson's scaling relations (Larson 1981), several authors (e. g., Myers et al. 1983; Caselli & Myers 1995; Pirogov et al. 2003) found, from single-dish studies, that larger dense cores have broader lines, as expected in virialised cores. In our sample, however, we find no correlation (with $\tau = -0.03$ and $\rho = 0.01$) between these two quantities. A possible explanation for this could be that a number of cores suffer an important injection of turbulence, e. g., from the passage of powerful outflows, which should affect the gas motions of the cores only at the scales of our sample ($\sim$ 0.05 pc; see e. g., Palau et al. 2007b; Liu et al. 2010; Nakamura & Li 2011), and is diluted at the larger scales studied in single-dish observations. Alternatively, the large linewidths might indicate that the cores are collapsing. In Sect. 4.2, we discuss in more detail the dynamics of the cores in our sample, and relate it to previous single-dish studies.

4 DISCUSSION

4.1 Temperature of the gas and IR radiation

In Sect. 3.3, we reported a correlation between the temperature of the cores and the luminosity of the region (see Fig. 3 panel A). These higher temperatures can result from various heating processes: (i) feedback from low-mass stars, e. g., molecular outflows, as found in some cores of AFGL 5142 or 20293+5932 (e. g., Zhang et al. 2002; Palau et al. 2007b); (ii) shocks from convergent flows (e. g., Csengeri et al. 2011a; Beltrán et al. 2012); (iii) feedback from high-mass stars, e. g., strong radiation (e. g., Li et al. 2003). In the following, we

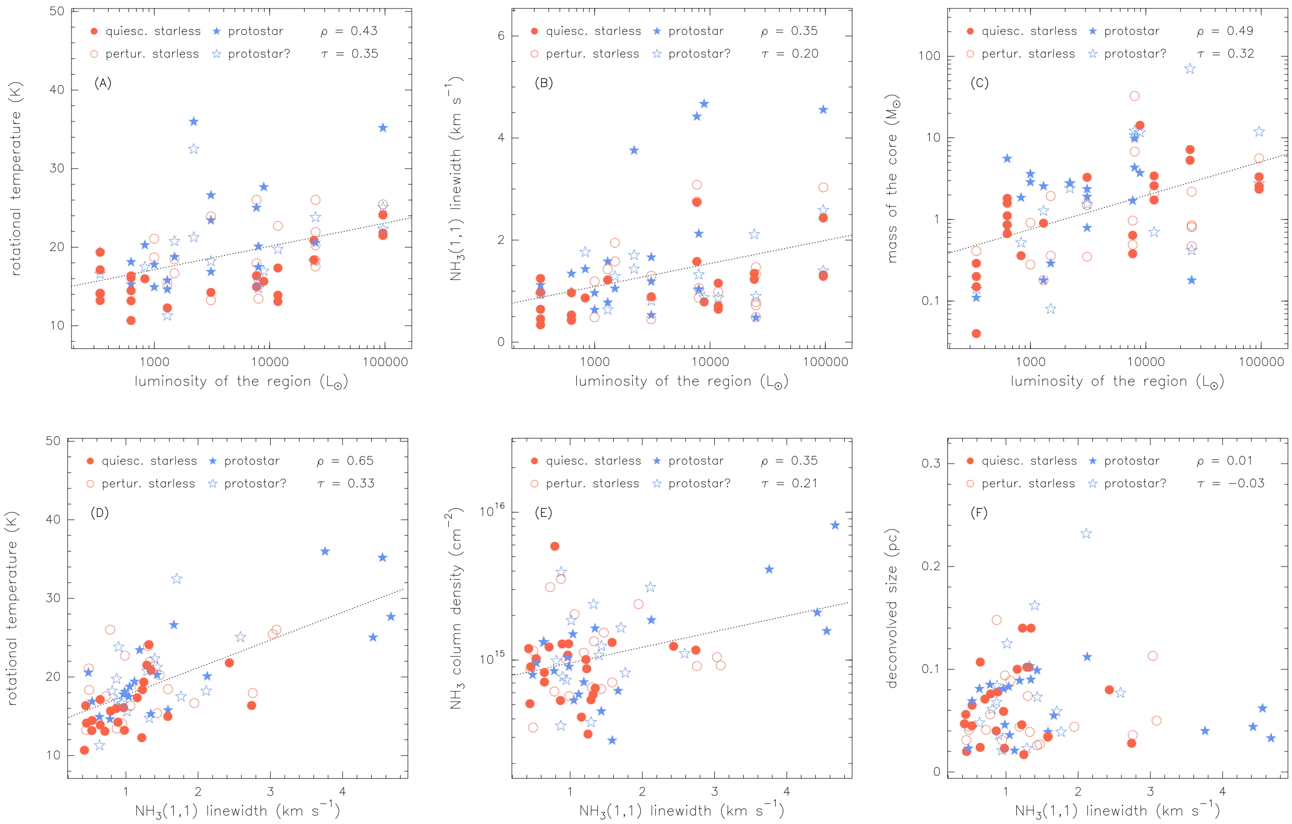

Figure 3. Scatter plots showing the correlations with respect to the bolometric luminosity of **(a)** the rotational temperature, **(b)** the NH_3 (1,1) linewidth, and **(c)** the core mass, in the top panels; and the correlations with respect to the linewidth of **(d)** the rotational temperature, **(e)** the ammonia column density, and **(f)** the core diametre. 'Quiescent starless' and 'perturbed starless' cores are shown in red filled and open circles respectively; while 'protostellar' and 'tentatively protostellar' cores are shown as blue filled and open stars, respectively (see Sect. 3.1 for details). The black dotted lines show the result of least-squares fits to the data (see Sect. 3.3), with the Pearson correlation coefficient (ρ) shown in the top right corner, together with Kendall's τ correlation coefficient.

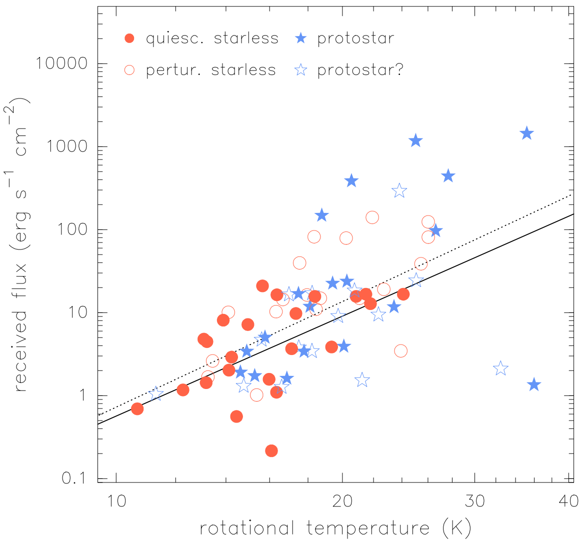

Figure 4. Received flux for each ammonia core versus the rotational temperature (see Sect. 4.1 for details). The dotted line shows a least-squares fit to the data, and the solid line corresponds to the relation $L_{\mathrm{bol}}/(4\pi(\Delta_{\mathrm{MIR-NH_3}})^2) = \sigma_{\mathrm{SB}}\, T_{\mathrm{rot}}^4$, with σ_{SB} the Stephan-Boltzmann constant. Symbols are as in Fig. 3.

test the feedback from massive stars as a possible agent for the increase of temperature in the dense cores.

Our interferometric observations permit the study of the spatial distribution of the cores, and their physical properties, with respect to, e. g., the (strong) infrared sources and hence the massive stars. In our regions, the bolometric luminosity is generally dominated, at mid-infrared (MIR) and far-infrared (FIR) wavelengths, by a single strong source associated with the most massive star. We assume that the main source of radiation that can heat the surrounding gas is the massive star detectable in the MIR. To determine if there is a relation between the temperature of the cores and the proximity of the MIR source, we searched the MSX Point Source Catalog (Price et al. 1999) for the coordinates of the MIR sources and calculated the MSX to NH_3 core separation ($\Delta_{\mathrm{MIR-NH_3}}$; using the coordinates listed in Table 3 for our cores). Using the luminosity and position of the most massive (radiating dominant) source and the separation to each ammonia dense core, we derived the incident flux received by each core as $L_{\mathrm{bol}}/(4\pi(\Delta_{\mathrm{MIR-NH_3}})^2)$. Note that we are measuring a projected separation, which is a lower limit to the true separation. Thus, for all cores, we actually have an upper limit on the received flux, which affects the absolute normalization of the derived relation and increases the scatter of the data points in this relation. In Fig. 4, we plot

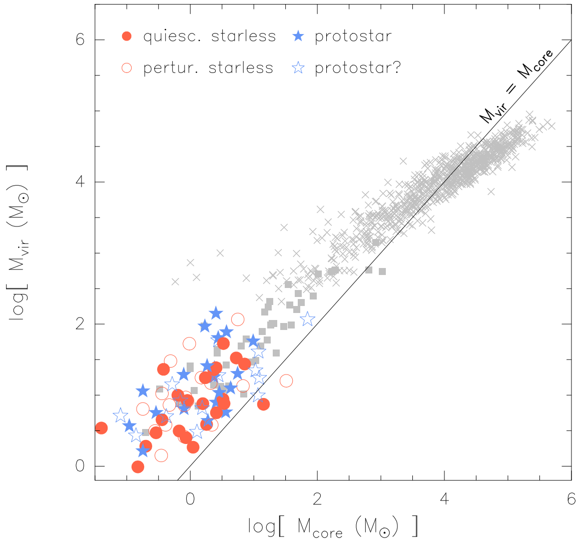

Figure 5. Scatter plot showing the relation between the virial mass $M_{\rm vir}$ (derived as $M_{\rm vir} = 210\,R\,\Delta v^2$; MacLaren et al. 1988) and the mass of the core $M_{\rm core}$. Blue-star and red-circle symbols correspond to the protostellar and starless cores studied in this work (symbols as in Fig. 3). Grey squares correspond to single-dish ammonia data (Sepúlveda et al. 2011) and grey crosses correspond to ^{13}CO single-dish data (Roman-Duval et al. 2010). The solid line corresponds to virialised cores with $M_{\rm vir} = M_{\rm core}$.

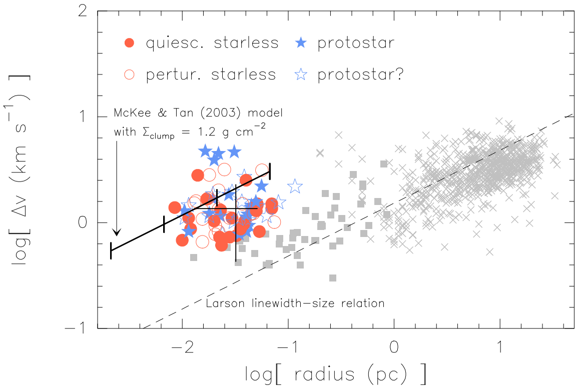

Figure 6. Variation of the linewidth, Δv, with core radius, following Csengeri et al. (2011b). Red and blue symbols correspond to the VLA ammonia data shown in this paper (see Fig. 3 for details), grey squares correspond to single-dish ammonia data (Sepúlveda et al. 2011), and grey crosses correspond to ^{13}CO single-dish data (Roman-Duval et al. 2010). The dashed line indicates a Larson like linewidth-size relation ($\Delta v \propto {\rm size}^{0.38}$). The thick solid line correspond to the turbulent regulated quasi-static model (McKee & Tan 2003), with a surface mass density of 1.3 g cm^{-2} and a core mass of 0.1 to 100 $M_\odot$ (each interval corresponds to 0.1, 1, 10, and 100 $M_\odot$). The black cross marks the mean and dispersion values of the linewidth (1.36 ± 0.93 km s^{-1}) and radius (0.032 ± 0.019 pc) for the cores studied in this work.

the received flux versus the rotational temperature. If the radiation of the most massive star dominates the heating of its surroundings, we expect that the cores closer to the most massive source, i. e., with a large received flux, will have higher temperatures. This is consistent with the trend shown in Fig. 4, where the highest temperatures correspond to the cores with a higher received flux. The black solid line corresponds to the relation $L_{\rm bol}/(4\pi(\Delta_{\rm MIR-NH_3})^2) = \sigma_{\rm SB}\,T^4_{\rm rot}$, with $\sigma_{\rm SB}$ the Stephan-Boltzmann constant, while the dotted line corresponds to a least-squares fit with a correlation coefficient of 0.6. For a given bolometric luminosity, the temperature is a factor of ~ 3 times lower for a core located at a distance ~ 0.5 pc, than for a similar core located at < 0.05 pc.

Summarising, the radiation deposited in the environment by the most luminous star of the cluster can be responsible for the temperatures measured in the cores of our clustered regions. Thus, the large temperatures measured for our starless cores, in comparison with the temperatures measured in low-mass star-forming regions, can be interpreted as external heating by the radiation of the most massive (forming) stars of the cluster.

4.2 Dynamical state of the cores

We estimated the virial mass of each core as $M_{\rm vir} = 210\,[R/{\rm pc}]\,[\Delta v/{\rm km~s^{-1}}]^2~M_\odot$ (MacLaren et al. 1988; see also Bertoldi & McKee 1992), where the numerical value accounts for an uniform density distribution across the core, and R and Δv are the radius of the core and the NH$_3$ (1,1) linewidth, respectively (both listed in Table 3). Note that this estimate considers the simplest case of virial equilibrium where only gravity and velocity dispersion of the gas are taken into account, thus neglecting the effects of, e. g., external pressure and magnetic fields. The calculated virial masses are listed in Col. 10 of Table 4. In Figure 5, we present a plot of virial mass, $M_{\rm vir}$, against the mass of the core derived from the ammonia emission, $M_{\rm core}$. In Fig. 5, we have also included the ammonia clumps studied by Sepúlveda et al. (2011) with the Haystack 37 m single-dish telescope (grey squares), and the ^{13}CO clouds of Roman-Duval et al. (2010) observed with the FCRAO 14 m single-dish telescope (grey crosses). These two samples permit to trace clumps at scales ~ 0.1–10 pc. From the plot we find that the trend outlined by this population of clumps is nicely followed by our NH$_3$ core population sampling lower masses, with the slope of the trend close to 1. This, in general, favors a scenario of a self-similar, self-gravitating, virialised hierarchy of structures from clumps to cores. The fact that the virial masses of almost all the cores at 0.05 pc (studied in this work) are several times larger than the core masses ($M_{\rm vir}/M_{\rm core} \sim 10$)[6]

---

[6] Note that the offset seen in Fig. 5 can not be easily explained in terms of the uncertainties of the observational quantities involved in the plot. The two main sources of uncertainty are the ammonia abundance and the linewidth. For the ammonia abundance we assumed a mean value of $(4.2\pm2.7)\times10^{-8}$. This value is obtained from different surveys (Pillai et al. 2006; Foster et al. 2009; Friesen et al. 2009; Rygl et al. 2010; Chira et al. 2013), over a total of 122 clumps of different star forming regions. Thus, we expect an uncertainty of $\sim 60\%$ for the mass of the core. The linewidth is obtained from the spectral line fit described in Sect. 3.2, which provides errors of a few tenths of km s^{-1}, corresponding to a 10–30% uncertainty in linewidth. These observational errors alone are expected to affect the data randomly instead of introducing a systematic offset, and thus are not likely the cause of the observed offset of about one order of magnitude.

suggests that the initial assumptions in our virial analysis might be too simplistic and that other mechanisms of support should be taken into account (e. g., external pressure, magnetic fields, large scale velocity gradients; see Mac Low & Klessen 2004; McKee & Ostriker 2007 and references therein). The turbulence-regulated quasi-static scenario proposed by McKee & Tan (2002, 2003) considers the effects of the external pressure and an internal pressure that is derived from a mixture of turbulence and large-scale magnetic fields, to characterise the evolution of dense cores until the formation of massive stars. Thus, a virialised core that is in pressure equilibrium with its natal self-gravitating clump has a mean velocity dispersion, $\sigma_{\rm vir}$, and a core radius, $R_{\rm vir}$, defined by

$$\left[\frac{\sigma_{\rm vir}}{\rm km~s^{-1}}\right] = 1.09 \left[\frac{M_{\rm core}}{60~M_{\odot}}\right]^{1/4} \left[\frac{\Sigma_{\rm clump}}{\rm g~cm^{-2}}\right]^{1/4}, \qquad (1)$$

$$\left[\frac{R_{\rm vir}}{\rm pc}\right] = 0.057 \left[\frac{M_{\rm core}}{60~M_{\odot}}\right]^{1/2} \left[\frac{\Sigma_{\rm clump}}{\rm g~cm^{-2}}\right]^{-1/2}, \qquad (2)$$

where the numerical values apply to the fiducial cores of McKee & Tan (2003) (see also Tan et al. 2013) with a power-law density distribution $\rho \propto r^{-k_\rho}$ with $k_\rho = 1.5$. $M_{\rm core}$ corresponds to the mass of the core, and $\Sigma_{\rm clump}$ is the mass surface density of the clump where the core is embedded, assumed to be equal to the external pressure (McKee & Tan 2003). In Fig. 6, we follow the approach of Csengeri et al. (2011b) to compare our observations (linewidth and core size) to the turbulent core model of McKee & Tan (2003) (represented by the thick black line). The turbulent dispersion and the size of the cores of the model have been computed for a 0.1 to 100 $M_{\odot}$ core mass, and adopting $\Sigma_{\rm clump} = 1.2$ g cm^{-2} as an average mass surface density of the clump, which has been estimated for our regions from single-dish (sub)millimetre continuum observations (see Table 6 for details). From Fig. 6, we find that the cores studied at scales of 0.05 pc have a mean and dispersion linewidth and radius of 1.36±0.93 km s^{-1} and 0.032±0.019 pc, respectively. These values, indicated by a black cross in Fig. 6, are slightly below the predictions of the turbulent core model, a result recently found also by Csengeri et al. (2011b) in a smaller sample of cores in the Cygnus-X region. This suggests that, when taking into account the external pressure effect at scales $\sim$ 0.05 pc, either other forms of support (e. g., strong magnetic fields at core scales) are required to stabilise the cores, or the cores are close to collapse or even collapsing. Observations to gather information on the magnetic field as well as on the internal kinematics of the cores should definitively confirm this picture of the NH$_3$ dense cores at 0.05 pc in our sample.

5 CONCLUSIONS

We present the results of VLA observations of the NH$_3$ (1,1) and (2,2) inversion transition lines towards a sample of 15 massive star-forming regions. We obtained an average spatial resolution of $\sim$ 0.05 pc, and analysed the ammonia emission in a consistent way. Our main conclusions can be summarised as follows:

Table 6. Parameters derived for the clumps associated with the 15 massive star-forming regions

#[a]	S_ν[b] (Jy)	Mass[c] ($M_{\odot}$)	FWHM[d] ($''$)	diametre[d] ($''$) / (pc)	$\Sigma_{\rm clump}$[e] (g cm^{-2})
1.	1.2	85	32.4	30.5 / 0.27	0.32
2.	15.3	278	28.7	25.1 / 0.22	1.55
3.	6.8	123	44.2	41.9 / 0.37	0.25
4.	21.1	384	40.2	37.7 / 0.33	0.94
5.	4.5	64	30.1	26.6 / 0.21	0.40
6.	7.3	199	31.9	28.7 / 0.31	0.57
7.	32.9	1160	30.0	26.5 / 0.32	2.97
8.	13.3	201	34.5	31.5 / 0.25	0.85
9.	28.3	2290	37.8	35.1 / 0.65	1.46
10.	15.2	341	45.0	42.8 / 0.42	0.53
11.	15.8	174	56.5	54.7 / 0.37	0.34
12.	6.7	253	38.5	35.9 / 0.45	0.33
13.	4.5	145	34.6	31.6 / 0.37	0.29
14.	5.2	17	16.5	8.8 / 0.03	4.30
15.	67.1	185	41.6	39.2 / 0.13	2.78

[a] Number of the region as indicated in Table 1.

[b] Flux density at 850 μm obtained from the SCUBA Legacy Project (Di Francesco et al. 2008), except for: 00117+6412 (region #1: 1.2 mm from IRAM 30 m, Sánchez-Monge et al. 2008); 20081+3122 (region #7: 850 μm from JCMT, Thompson et al. 2006); 22198+6336 (region #14: 850 μm from JCMT, Jenness et al. 1995).

[c] Mass of the clump measured from the JCMT at 850 μm or the IRAM 30 m at 1.2 mm, assuming a dust temperature of 20 K, a dust (+gas) mass opacity coefficient of 0.0175 cm^2 g^{-1} at 850 μm and 0.0090 cm^2 g^{-1} at 1.2 mm (Ossenkopf & Henning 1994), and a gas-to-dust mass ratio of 100.

[d] Observed diametre at full width half maximum obtained (FWHM) from a Gaussian fit, and deconvolved diametre derived taking into account a main beam for the SCUBA observations at 850 μm of 14$''$. Our sizes obtained from a Gaussian fit are slightly different to those reported by Palau et al. (2013), which were estimated by measuring the observed diametre directly on the image, and using a beam size of 23$''$ for deconvolution, which affects mainly the sources with the smallest sizes.

[e] Clump mass surface density derived as $\Sigma_{\rm clump}$ = Mass/Area with Area = π (diametre/2)^2.

- We identified a total of 73 ammonia dense cores using the two-dimensional CLUMPFIND algorithm. On average we found of the order of 5–6 cores in each field (of $\sim$ 2 arcmin, or 1.5 pc at a distance of 2.5 kpc), with sizes $\sim$ 0.06 pc. The cores were classified as quiescent starless, perturbed starless, and protostellar based on its association with infrared emission and taking into account other star formation signposts (e. g., outflows, masers, centimetre continuum emission) reported in the literature.

- The average values of linewidth, opacity, rotational temperature, and ammonia column density for the 73 dense cores are $\sim$ 1.4 km s^{-1}, 1.4, 19 K, and 10^{15} cm^{-2}, respectively. We found that protostellar cores have larger temperatures and linewidths ($\sim$ 21.3 K and 1.8 km s^{-1}) than quiescent starless cores ($\sim$ 16.0 K and 1.0 km s^{-1}). Similarly, cores classified as perturbed starless have temperatures and linewidths ($\sim$ 19.3 K and 1.4 km s^{-1}) slightly larger than quiescent starless cores, but smaller than cores harboring a protostar.

- The average temperatures derived for the quiescent starless cores in our clustered regions ($\sim$ 16 K) are larger than those measured in starless cores in more isolated regions ($\sim$ 10 K). Our starless and protostellar cores show important non-thermal supersonic components ($\sigma_{\rm nth} \sim 0.44$ km s^{-1} and 0.76 km s^{-1}, respectively) and $\sigma_{\rm nth}/c_s \sim 2.0$, well above to the close-to-thermal lines measured in isolated star-forming regions.

- We found that the temperature and NH_3 (1,1) linewidth of the cores are correlated with the luminosity of the region, suggesting that the feedback of the luminous massive (forming) stars can affect the surrounding molecular environment.

- We evaluated a possible relation between the temperature of the core and its separation with the most important radiating source in the region, in terms of the incident flux received by the core. The highest temperatures are measured for those cores located close to the brightest MIR source (separations < 0.05 pc), with the temperature decaying by a factor of ~ 3 when the cores are located at distances ~ 0.5 pc. Thus, the large temperatures found in starless cores in massive star-forming regions, can be interpreted as external heating by the radiation of most the massive star of the cluster.

- We compared the virial masses of our cores (at scales ~ 0.05 pc) with those of clumps with sizes $\sim$ 0.1–10 pc. A simple virial equilibrium analysis seems to suggest a trend between $M_{\rm vir}$ and core/clump masses favoring a scenario of a self-similar, self-graviting, virialised hierarchy of structures from clumps to cores. A closer inspection of the dynamical state at core scales, taking into account external pressure (McKee & Tan 2003), indicates that either another form of support (e. g., from magnetic field) is required to stabilise the cores, or that the cores are close to collapse or even collapsing.

Overall, our data suggest that the cores forming in clustered environments harboring intermediate/high-mass stars are more affected/perturbed than cores in clustered low-mass star-forming regions, and thus the initial conditions for star formation in these environments seem to be different to those typically assumed in low-mass star-forming regions.

ACKNOWLEDGMENTS

We are grateful to James di Francesco for support with SCUBA data. We thank the anonymous referee for his/her constructive criticisms. The figures of this paper have been done in GREG of the GILDAS software package developed at the Institut de Radioastronomie Millimétrique (IRAM) and the Observatoire de Grenoble. A.P. is supported by a JAE-Doc CSIC fellowship co-funded with the European Social Fund under the program 'Junta para la Ampliación de Estudios', by the Spanish MICINN grant AYA2011-30228-C03-02 (co-funded with FEDER funds), and by the AGAUR grant 2009SGR1172 (Catalonia). G.B. is funded by an Italian Space Agency (ASI) fellowship under contract number I/005/11/0.

REFERENCES

André P., Belloche A., Motte F., Peretto N. 2007, A&A, 472, 519
Avni Y. 1976, ApJ, 210, 642
Beltrán M. T., Massi F., Fontani F., Codella C., & López R. 2012, A&A, 542, L26
Bergin E. A., & Tafalla M. 2007, ARA&A, 45, 339
Bertoldi F., & McKee C. F. 1992, ApJ, 395, 140
Beuther H., Schilke P., Gueth F., McCaughrean M., Andersen M., Sridharan T. K., Menten K. M. 2002a, A&A, 387, 931
Beuther H., Schilke P., Menten K. M., et al. 2002b, ApJ, 566, 945
Beuther H., Schilke P., Gueth F., et al. 2002c, A&A, 387, 931
Beuther H., Walsh A., Schilke P., et al. 2002d, A&A, 390, 289
Beuther H., Schilke P., & Gueth F. 2004a, ApJ, 608, 330
Beuther H., Schilke P., & Wyrowski F. 2004b, ApJ, 615, 832
Beuther H., Leurini S., Schilke P., et al. 2007, A&A, 466, 1065
Briggs D. 1995, Ph.D. Thesis, New Mexico Inst. of Mining and Technology
Busquet G., Palau A., Estalella R., et al. 2009, A&A, 506, 1183
Busquet G., Palau A., Estalella R., et al. 2010, A&A, 517, L6
Busquet G. 2010, Ph.D. Thesis, Universitat de Barcelona
Busquet G., Estalella R., Zhang Q., et al. 2011, A&A, 525, A141
Caselli P., & Myers P. C. 1995, ApJ, 446, 665
Caselli P., Walmsley C.M., Zucconi A. et al. 2002, ApJ, 565, 344
Cesaroni R., Felli M., Testi L., Walmsley C. M., & Olmi L. 1997, A&A, 325, 725
Cesaroni R., Felli M., Jenness T., et al. 1999, A&A, 345, 949
Cesaroni R., Neri R., Olmi L., et al. 2005, A&A, 434, 1039
Chira R.-A., Beuther H., Linz H., et al. 2013, A&A, 552, A40
Churchwell E., Walmsley C. M., & Cesaroni R. 1990, A&AS, 83, 119
Crapsi A., Caselli P., Walmsley C.M., et al. 2005, ApJ, 619, 379
Csengeri T., Bontemps S., Schneider N., et al. 2011a, ApJL, 740, L5
Csengeri T., Bontemps S., Schneider N., Motte F., & Dib S. 2011b, A&A, 527, A135
Di Francesco J., Johnstone D., Kirk H., MacKenzie T., & Ledwosinska E. 2008, ApJS, 175, 277
Estalella R., Mauersberger R., Torrelles J. M., et al. 1993, ApJ, 419, 698
Estalella R., López R., Anglada G., et al. 2012, ApJ, 144, 61
Fontani F., Cesaroni R., Testi L., et al. 2004, A&A, 424, 179
Fontani F., Caselli P., Bourke T. L., Cesaroni R., Brand J. 2008, A&A, 477, L45
Fontani F., Zhang Q., Caselli P., Bourke T. L. 2009, A&A, 499, 233

Fontani F., Palau A., Caselli P., et al. 2011, A&A, 529, L7
Fontani F., Caselli P., Zhang Q., et al. 2012a, A&A, 541, A32
Fontani F., Palau A., Busquet G., et al. 2012b, MNRAS, 423, 1691
Foster J. B., Rosolowsky E. W., Kauffmann J., et al. 2009, ApJ, 696, 298
Friesen R. K., Di Francesco J., Shirley Y. L., Myers P. C. 2009, ApJ, 697, 1457
Gutermuth R. A., Megeath S. T., Myers P. C., et al. 2009, ApJS, 184, 18
Halton J. H. 1964, Commun. ACM, 7, 701
Ho P. T. P., & Townes C. H. 1983, ARA&A, 21, 239
Jenness T., Scott P. F., & Padman R. 1995, MNRAS, 276, 1024
Jijina J., Myers P. C., & Adams F. C. 1999, ApJSS, 125, 161
Keto E., & Zhang Q. 2010, MNRAS, 406, 102
Khanzadyan T., Movsessian T. A., Davis C. J., et al. 2011, MNRAS, 418, 1994
Kumar M. S. N., Tafalla M., & Bachiller R. 2004, A&A, 426, 195
Lampton M., Margon B., & Bowyer S. 1976, ApJ, 208, 177
Leurini S., Beuther H., Schilke P., et al. 2007, A&A, 475, 925
Li D., Goldsmith P. F., & Menten K. 2003, ApJ, 587, 262
Liu H. B., Ho P. T. P., & Zhang Q. 2010, ApJ, 725, 2190
Mac Low M.-M., & Klessen R. S. 2004, Reviews of Modern Physics, 76, 125
MacLaren I., Richardson K. M., & Wolfendale A. W. 1988, ApJ, 333, 821
McKee C. F., & Ostriker E. C. 2007, ARA&A, 45, 565
McKee C. F., & Tan J. C. 2002, Nature, 416, 59
McKee C. F., & Tan J. C. 2003, ApJ, 585, 850
Miettinen O., Harju J., Haikala L. K., & Juvela M. 2012, A&A, 538, A137
Molinari S., Brand J., Cesaroni R., & Palla F. 1996, A&A, 308, 573
Molinari S., Testi L., Rodríguez L. F., & Zhang Q. 2002, ApJ, 570, 758
Molinari S., Pezzuto S., Cesaroni R., et al. 2008, A&A, 481, 345
Molinari S., Swinyard B., Bally J., et al. 2010, PASP, 122, 314
Motte F., Zavagno A., Bontemps S., et al. 2010, A&A, 518, L77
Mueller K. E., Shirley Y. L., Evans N. J., II, & Jacobson H. R. 2002, ApJS, 143, 469
Myers P. C., Linke R. A., & Benson P. J. 1983, ApJ, 264, 517
Myers P. C., Ladd E. F., Fuller G. A. 1991, ApJ, 372, L95
Nakamura M. & Li Z.-Y. 2007, ApJ, 662, 395
Nakamura F. & Li Z.-Y. 2011, ApJ, 740, 36
Neugebauer G., Habing H. J., van Duinen R., et al. 1984, ApJL, 278, L1
Olmi L., Anglés-Alcázar D., Elia D., et al. 2013, A&A, 551, A111
Ossenkopf, V., & Henning, T. 1994, A&A, 291, 943
Palau A., Estalella R., Ho P. T. P., Beuther H., & Beltrán M. T. 2007a, A&A, 474, 911
Palau A., Estalella R., Girart J. M., et al. 2007b, A&A, 465, 219
Palau A., Sánchez-Monge Á., Busquet G., et al. 2010, A&A, 510, A5
Palau A., Fuente A., Girart J. M., et al. 2011, ApJL, 743, L32
Palau A., Fuente A., Girart J. M., et al. 2013, ApJ, 762, 120
Patel N. A., Curiel S., Sridharan T. K., et al. 2005, Nature, 437, 109
Pauls A., Wilson T. L., Bieging J. H., & Martin R. N. 1983, A&A, 124, 23
Pillai T., Wyrowski F., Carey S. J., & Menten K. M. 2006, A&A, 450, 569
Pillai T., Kauffmann J., Wyrowski F., et al. 2011, A&A, 530, A118
Pirogov L., Zinchenko I., Caselli P., Johansson L. E. B., & Myers P. C. 2003, A&A, 405, 639
Price S. D., Egan M. P., Mizuno D. R., Kuchar T. A., & Carey S. J. 1999, Bulletin of the American Astronomical Society, 31, 1515
Ragan S. E., Bergin E. A., Wilner D. 2011, ApJ, 736, 163
Rathborne J. M., Lada C. J., Muench A. A., Alves J. F., & Lombardi M. 2008, ApJSS, 174, 396
Rodriguez L. F., Moran J. M., Ho P. T. P., & Gottlieb E. W. 1980, ApJ, 235, 845
Roman-Duval J., Jackson J. M., Heyer M., Rathborne J., & Simon R. 2010, ApJ, 723, 492
Rosolowsky E. W., Pineda J. E., Foster J. B., et al. 2008, ApJSS, 175, 509
Rygl K. L. J., Wyrowski F., Schuller F., & Menten K. M. 2010, A&A, 515, A42
Sánchez-Monge Á., Palau A., Estalella R., Beltrán M. T., & Girart J. M. 2008, A&A, 485, 497
Sánchez-Monge Á., Palau A., Estalella R., et al. 2010, ApJL, 721, L107
Sánchez-Monge Á. 2011, Ph.D. Thesis, Universitat de Barcelona
Sánchez-Monge Á., Kurtz S., Palau A., et al. 2013, ApJ, 766, 114
Schnee S., Enoch M., Noriega-Crespo A., et al. 2010, ApJ, 708, 127
Sepúlveda I., Anglada G., Estalella R., et al. 2011, A&A, 527, A41
Su Y.-N., Liu S.-Y., & Lim J. 2009, ApJ, 698, 1981
Tafalla M., Myers P. C., Caselli P., Walmsley C. M., Comito C. 2002, ApJ, 569, 815
Tafalla M., Myers P. C., Caselli P., Walmsley C. M. 2004, A&A, 416, 191
Tan J. C., Kong S., Butler M. J., Caselli P., & Fontani F. 2013, arXiv:1303.4343
Testi L., Palla F., & Natta A. 1999, A&A, 342, 515
Thompson M. A., Hatchell J., Walsh A. J., MacDonald G. H., & Millar T. J. 2006, A&A, 453, 1003
Torrelles J. M., Ho P. T. P., Rodriguez L. F., Canto J. 1986, ApJ, 305, 721
Urquhart J. S., et al. 2011, MNRAS, 418, 1689
Varricatt W. P., Davis C. J., Ramsay S., & Todd S. P. 2010, MNRAS, 404, 661
Wall J. V., & Jenkins C. R. 2003, Practical statistics for astronomers, by J.V. Wall and C.R. Jenkins. Cambridge observing handbooks for research astronomers, vol. 3. Cambridge, UK: Cambridge University Press, 2003, Ed. R. Ellis, J. Huchra, S. Kahn, G. Rieke, P. B. Stetson

Wang Y., Zhang Q., Pillai T., Wyrowski F., Wu, Y. 2008, ApJ, 672L, 33

Ward-Thompson D., André P., Crutcher R. 2007, PPV conference, 951, p. 33

Williams J. P., de Geus E. J., & Blitz L. 1994, ApJ, 428, 693

Wright E. L., Eisenhardt P. R. M., Mainzer A. K., et al. 2010, AJ, 140, 1868

Zhang Q., Hunter T. R., Sridharan T. K., & Ho P. T. P. 2002, ApJ, 566, 982

Zhang Q., Hunter T. R., Beuther H., et al. 2007, ApJ, 658, 1152

APPENDIX A: HYPERFINE STRUCTURE (HFS) FITTING

A1 Parameters of the fit

The usual fitting of the hyperfine structure of a transition, for instance, the inversion transition NH_3 $(J, K) = (1, 1)$, estimates four free parameters of the transition, namely

i) τ_m, the optical depth of the main component,
ii) $A \times \tau_m$, product of the amplitude ($A = f[J_\nu(T_{\rm ex}) - J_\nu(T_{\rm bg})]$, where f is the filling factor, $J_\nu(T)$ is the Planck function in units of temperature, $T_{\rm ex}$ is the excitation temperature, and $T_{\rm bg}$ is the background temperature) times the optical depth of the main component,
iii) $v_{\rm LSR}$, the central velocity of the main component, and
iv) Δv, the linewidth of the hyperfine components,

with the usual assumptions that $T_{\rm ex}$, $v_{\rm LSR}$, and Δv are the same for all the hyperfine components.

However, some of the parameters are ill-conditioned in some cases. In the optically thin limit, $\tau_m \ll 1$, only an upper limit for the value of τ_m can be obtained. However, the parameter $A \times \tau_m$ gives the peak intensity of the line (provided that the hyperfine components are unresolved, or, in the case NH_3, the hyperfine magnetic components that form part of the main component), and is well constrained. This parameter, in the Rayleigh-Jeans approximation, is necessary to calculate the column density of emitting molecules. In the optically thick limit, $\tau_m \gg 1$, only lower limits for τ_m and $A \times \tau_m$ can be obtained (and consequently, a lower limit for the column density).

A better fit parameter than τ_m, with well defined values in the optically thin and optically thick limits, is $1 - e^{-\tau_m}$. This parameter always has values between 0 (optically thin limit, $\tau_m \ll 1$) and 1 (optically thick limit, $\tau_m \gg 1$). Similarly, $A\left(1 - e^{-\tau_m}\right)$ is a better fit parameter than $A \times \tau_m$, since it is well constrained in all cases.

The Hyperfine Structure[7] (hereafter HfS) fitting procedure used to fit the NH_3 $(J, K) = (1, 1)$ lines in this paper, fits the four parameters

i) $1 - e^{-\tau_m}$,
ii) $A\left(1 - e^{-\tau_m}\right)$,
iii) $v_{\rm LSR}$,
iv) Δv.

Table A1. Values of $\Delta(m, \alpha)$ for calculating the parameter uncertainties, where m is the number of fitted parameters simultaneously, and α is the significance level, given in percent and in the equivalent number of sigmas for a Gaussian error distribution.

	α			
m	68.23% (1σ)	90.00% (1.64σ)	99.00% (2.57σ)	99.90% (3.30σ)
1	1.00	2.71	6.64	10.83
2	2.30	4.60	9.21	13.82
3	3.53	6.25	11.34	16.27
4	4.72	7.78	13.28	18.46
5	5.89	9.24	15.09	20.52
6	7.04	10.64	16.81	22.46
7	8.17	12.02	18.48	24.32
8	9.30	13.36	20.09	26.12
9	10.42	14.68	21.67	27.87
10	11.53	15.99	23.21	29.59

The values and uncertainties for the parameters needed to derive physical properties of the emitting gas, τ_m and $A \times \tau_m$ (or their limits in the two limiting cases) can be easily derived from the values and uncertainties for the parameters of the fit.

A2 Fitting procedure

The fitting strategy was similar to that used by Estalella et al. (2012). HfS samples the parameter space of dimension four, defined by the parameters $1 - e^{-\tau_m}$, $A\left(1 - e^{-\tau_m}\right)$, $v_{\rm LSR}$, and Δv, to find the minimum value of χ^2,

$$\chi^2 \equiv \sum_{i=1}^{n} \left[\frac{y_i^{\rm obs} - y_i^{\rm mod}(p_1, \ldots, p_m)}{\sigma_i} \right]^2, \tag{A1}$$

where $y_i^{\rm obs}$ are the observed line intensities for the n spectral channels, $y_i^{\rm mod}(p_1, \ldots, p_m)$ are the model line intensities, depending on m free parameters p_k, and σ_i are the errors of the observations.

If the model is a good fit to the observations, χ^2 has a minimum value given by

$$\chi^2_{\rm min} \simeq n - m. \tag{A2}$$

This can be used to estimate the observational error, σ (the same for all points), if unknown,

$$\sigma^2 \simeq \frac{1}{n - m} \sum_{i=1}^{n} \left[y_i^{\rm obs} - y_i^{\rm mod} \right]^2. \tag{A3}$$

Several sampling methods of the m-dimensional parameter space are possible, i. e., regular grid, random, Halton sequence (Halton 1964). We adopted a Halton quasi-random sequence because it samples the parameter space more evenly than a purely random sequence, and the convergence of the fitting procedure to the minimum of χ^2 is faster.

A3 Parameter error estimation

Once the best fit parameter values for which $\chi^2 = \chi^2_{\rm min}$ are found, the uncertainty in the fitted parameters, $\sigma(p_k)$,

---

[7] HfS is freely available and can be downloaded from http://www.am.ub.edu/∼robert/hfs/hfs.html

($k = 1 \ldots m$), can be estimated as the projection over each parameter axis of the confidence region of the parameters, the region of the m-dimensional parameter space for which χ^2 does not exceed the minimum value by a certain amount, $\chi^2_{\rm min} + \Delta$.

Following Avni (1976) and Wall & Jenkins (2003), the probability

$$\mathrm{Prob}\left[\chi^2 - \chi^2_{\rm min} \leqslant \Delta(m, \alpha)\right] = \alpha, \tag{A4}$$

is that of a chi-square distribution with m degrees of freedom, and α is the significance level ($0 < \alpha < 1$). Thus, $\Delta(m, \alpha)$ is the increment in χ^2 such that if the observation is repeated a large number of times, a fraction α of times the values of the fitted parameters will be inside the confidence region, i.e. in the interval $p_k \pm \sigma(p_k)$. For instance, in the case of this paper, $m = 4$, and for a significance level of 0.68 (equivalent to 1 σ for a Gaussian error distribution), the value of the increment in $\chi^2_{\rm min}$ is $\Delta(4, 0.68) = 4.72$ (Lampton et al. 1976; see Table A1).

Assuming that the model is a good fit to the observations, i. e., $\chi^2_{\rm min} \simeq n - m$, the condition

$$\chi^2 = \chi^2_{\rm min} + \Delta(m, \alpha), \tag{A5}$$

can be written as

$$\frac{\chi^2}{\chi^2_{\rm min}} \simeq 1 + \frac{\Delta(m, \alpha)}{n - m}. \tag{A6}$$

This expression is useful since it can be given in terms of the rms fit residual, ϵ,

$$\epsilon^2 \equiv \frac{\sum_{i=1}^{n} \left[(y_i^{\rm obs} - y_i^{\rm mod})/\sigma_i\right]^2}{\sum_{i=1}^{n} 1/\sigma_i^2} = \frac{\chi^2}{\sum_{i=1}^{n} 1/\sigma_i^2}, \tag{A7}$$

for which we obtain that the confidence region is given by the parameter values that increase the rms fit residual to

$$\epsilon \simeq \epsilon_{\rm min} \sqrt{1 + \frac{\Delta(m, \alpha)}{n - m}}. \tag{A8}$$

This last expression can be used even when the errors of the observations are unknown.

APPENDIX B: VELOCITY, LINEWIDTH AND SPECTRA IMAGES

In Table B1, we summarize the infrared properties of each core, together with the information of other star formation signposts reported in the literature. In Col. 4 of the table, we classify each core as 'quiescent starless' (S), 'perturbed starless' (S*), 'protostellar' (P) or 'tentatively protostellar' (P?).

In Fig. B1, we present the first-order (intensity weighted mean $v_{\rm LSR}$) and second-order (intensity weighted mean linewidth) moment maps for the 15 massive star-forming regions studied in this work. Note that the second-order moment maps have been corrected to show directly the linewidth (Δv) instead of the dispersion (σ_v), by using the relation $\Delta v = \sqrt{8 \ln 2}\, \sigma_v$.

In Fig. B2, we present the observed and fitted spectra of the $\mathrm{NH_3}$ (1,1) and $\mathrm{NH_3}$ (2,2) transitions for all the cores identified and listed in Table 3.

Table B1. Classification of ammonia cores in protostellar or starless

`ID` Region^{a}	#	Type^{b}	IRAC	MIPS/WISE	mm	cm	outflow	maser	comments
01 00117+6412	01	P	point	-	yes	no	no	no	
02	02	S	dark	-	yes	no	no	no	
03	03	P	point	yes	yes	yes	yes	yes	
04	04	S*	dark	-	yes	no	no	yes	
05	05	P?	point	-	no	no	no	no	no mm/outflow/maser associated
06 AFGL5142	01	P	point	yes	yes	yes	yes	yes	
07	02	P?	point	-	no	no	OA	no	core along outflow axis
08	03	P?	point	-	no	no	no	no	
09 05345+3157NE	01	P	point	-	yes	yes	no?	no	
10	02	P	point	yes	yes	no	yes	yes	
11	03	S	dark	-	no	no	no	no	
12	04	S	dark?	yes?	yes	no	no	no	point IR source at the border, but dark
13	05	S	dark	-	yes	no	no	no	
14	06	S	dark	-	yes	no	no	no	
15	07	S	dark	-	no	no	no	no	
16 05358+3543NE	01	P	ext?	-	yes	no	yes	no	
17	02	P?	point	-	no	no	OA	no	core along outflow axis
18	03	P	point	yes	yes	yes	yes	yes	
19	04	S*	dark	-	no	no	OA	no	near CO outflow lobe
20	05	P	point	-	no	no	yes	no	
21	06	S*	dark	-	no	no	OA	no	near SiO outflow lobe
22	07	S	dark	-	no	no	no	no	
23 05373+2349	01	P	point	-	yes	yes	yes	no	
25	02	S*	dark?	yes?	faint	no	no	no	between two strong IR sources
27 19035+0641	01	P	point	yes		yes			
28	02	S*	dark	-		no			close to bright IRAC source
29	03	S	dark	-		no			
30	04	S?	ext	-		no			
31	05	S	dark	-		no			
32 20081+3122	01	P?	point	-	yes?	no	OA	no	mm source 4″ to the south of the polygon
33	02	S	dark	-	no	no	no	no	
35 20126+4104	01	P	point	yes	yes	yes	yes	yes	
36	02	S	dark	-	yes	no	no	no	
37	03	P?	point	-	no	no	no	no	
38 G75.78+0.34	01	P	point	yes	yes	yes	yes	yes	
39	02	S*	ext	-	no	no	no	no	near strong IRAC source
40	03	P?	point	-	no	no	no	no	
41	04	S	dark	-	no	no	no	no	
43	05	S	dark	-	no	no	no	no	
44	06	P?	point	-	no	no	no	no	
45 20293+3952	01	S*	dark?	-	no	no	no	no	near strong IRAC source
46	02	S*	dark?	-	yes	no	OA	no	perturbed by outflow
47	03	P	point	yes	yes	no	yes	yes	
48	04	P?	point	-	yes	no	no	no	
49	05	P	point	yes	yes	no	yes	no	
50	06	P?	point	-		no	no		
51 20343+4129	01	S*	ext	-	yes	no	no	no	near strong IRAC source, perturbed?
52	02	S*	dark	-	yes	no	OA?	no	near strong IRAC source, perturbed?
53	03	P?	dark?	-	yes	yes?	OA?	no	near strong IRAC source, perturbed?
54	04	P	point	yes	faint	yes	no	no	
55 22134+5834	01	S	dark	-		no		no	
56	02	S*	dark?	-		no		no	near strong IRAC source, perturbed?
57	03	S	dark	-		no		no	
58	04	S	dark	-		no		no	
59	05	P?	point	-		no		no	

Table B1 – *continued*

ID	Region[a]	#	Type[b]	IRAC	MIPS/WISE	mm	cm	outflow	maser	comments
60	22172+5549N	01	P	point	yes	yes	no	yes	no	
61		02	S	dark	-	no	no	no	no	
62		03	P?	point	yes	faint	no	OA	no	core along outflow axis
63	22198+6336	01	S	dark	-	no	no	no	no	
64		02	P?	point	-	no	no	no	no	
65		03	P	point	yes	yes	yes	yes	yes	
66		04	S*	ext	-	no	no	OA	no	core along outflow axis
67		05	S	dark	-	no	no	no	no	
68		06	S	dark	-	no	no	no	no	
69		07	S	dark	-	yes	no	no	no	
70		08	S	dark	-		no		no	
71	CepA	01	S*	dark	-		no	OA	no	core close to outflow axis
72		02	S*	dark	-		no	no	no	
73		03	S*	dark	-		no	OA	no	core close to outflow axis
74		04	P?	point	-		no	OA	no	core close to outflow axis
75		05	S*	ext	-		no	OA	no	core close to outflow axis
76		06	S?	ext	-		no	no	no	
77		07	P	point	yes		no	OA	no	core close to outflow axis

[a] References: We have made use of the *Spitzer*/IRAC, *Spitzer*/MIPS, and WISE images to characterise the IR properties of the cores at wavelengths ranging from 3.6 μm to 24 μm. For each region we have searched the literature for information on millimeter continuum, centimetre continuum, outflow and maser emission. The references used (for each region) are:
00117+6412: Palau et al. (2010); Busquet (2010); Sánchez-Monge (2011);
AFGL5142: Zhang et al. (2002, 2007); Busquet (2010); Sánchez-Monge (2011); Busquet et al. (2011); Palau et al. (2011, 2013);
05345+3157NE: Fontani et al. (2008, 2009, 2012a);
05358+3543NE: Beuther et al. (2002c, 2007); Leurini et al. (2007); Sánchez-Monge (2011);
05373+2349: Rodriguez et al. (1980); Varricatt et al. (2010); Molinari et al. (1996, 2002, 2008); Gutermuth et al. (2009); Khanzadyan et al. (2011);
19035+0641: Sánchez-Monge (2011);
20081+3122: Su et al. (2009); Kumar et al. (2004);
20126+4104: Cesaroni et al. (1997, 1999, 2005); Keto & Zhang (2010); Busquet (2010);
G75.78+0.34: Sánchez-Monge (2011); Sánchez-Monge et al. (2013);
20293+3952: Beuther et al. (2002d, 2004a,b); Palau et al. (2007a);
20343+4129: Palau et al. (2007b); Fontani et al. (2012b);
22134+5834: Busquet (2010); Sánchez-Monge (2011);
22172+5549N: Fontani et al. (2004); Palau et al. (2011, 2013);
22198+6336: Sánchez-Monge et al. (2010); Sánchez-Monge (2011); Palau et al. (2011, 2013);
CepA: Torrelles et al. (1986); Patel et al. (2005).

[b] Type of the core: S: quiescent starless, S*: perturbed starless, P: protostellar, P?: tentatively protostellar (see Sect. 3.1).

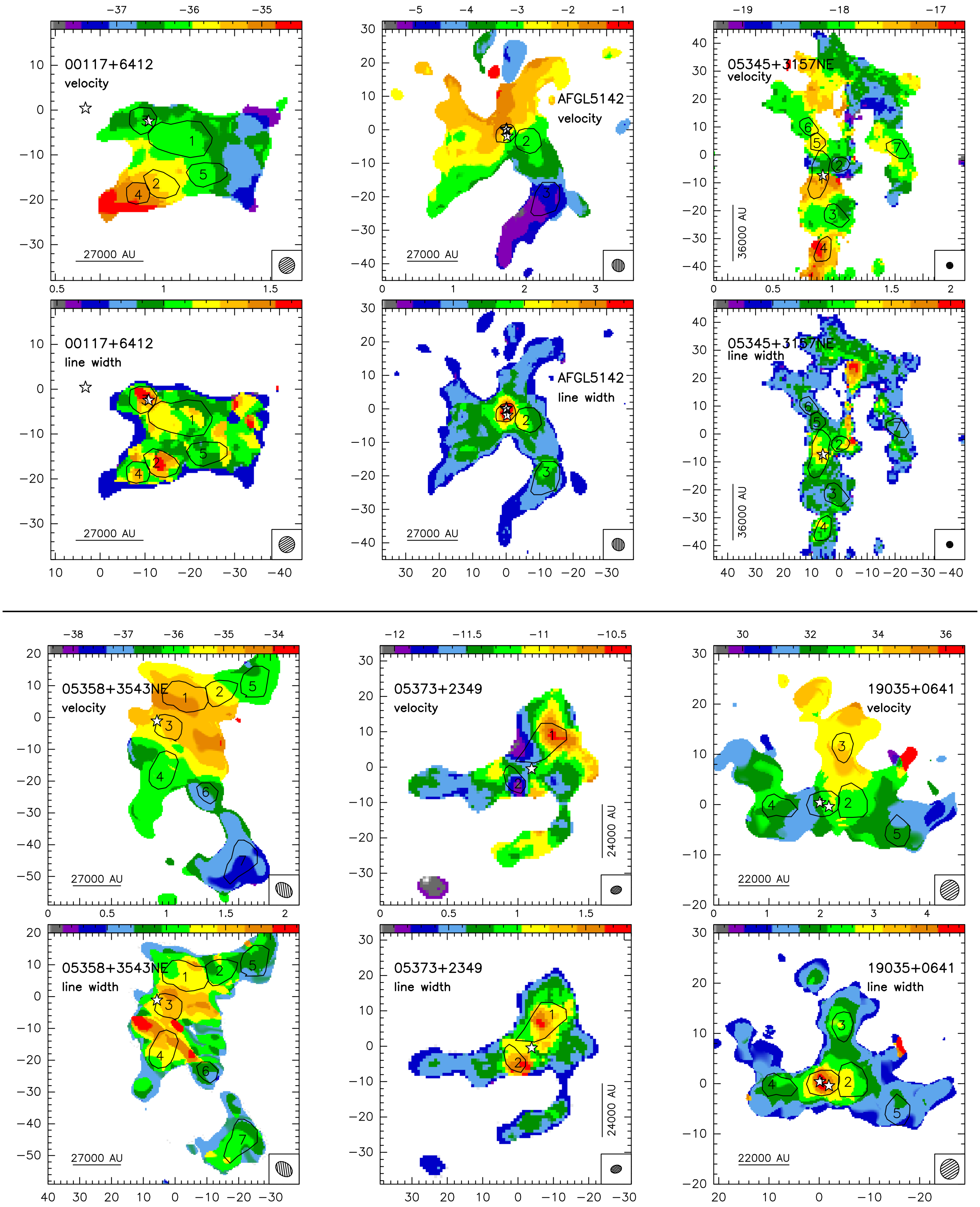

Figure B1. Velocity and linewidth maps (in units of km s^{-1}) obtained from the first and second-order moment maps. Note that the second-order moment map has been multiplied by $\sqrt{8 \ln 2}$ to obtain linewidth instead of dispersion. For each region we show two panels corresponding to the intensity weighted mean $v_{\rm LSR}$ (top panel) and to the intensity weighted mean velocity linewidth (bottom panel). Colour scales are indicated in the top of each panel. Symbols are as in Fig. 1.

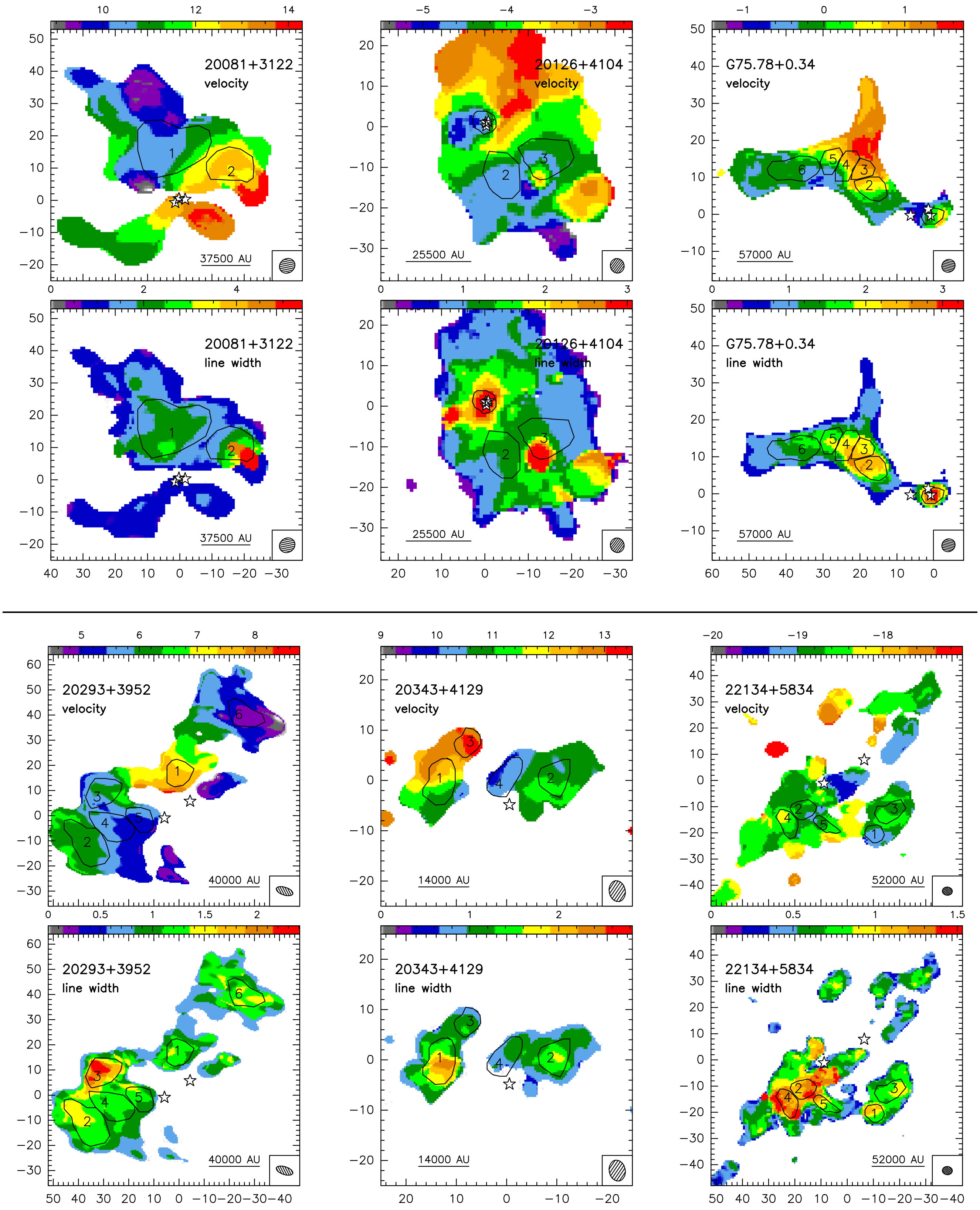

Figure B1 – *continued*

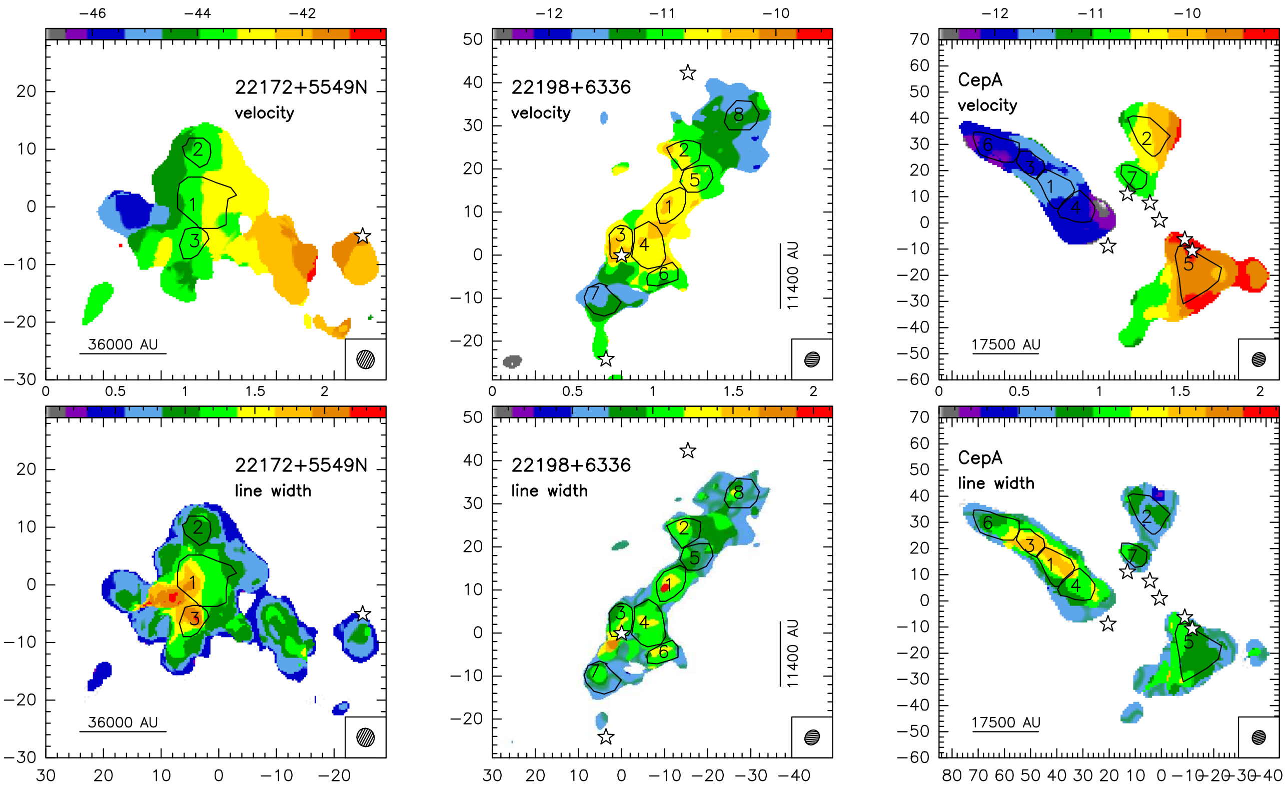

Figure B1 – *continued*

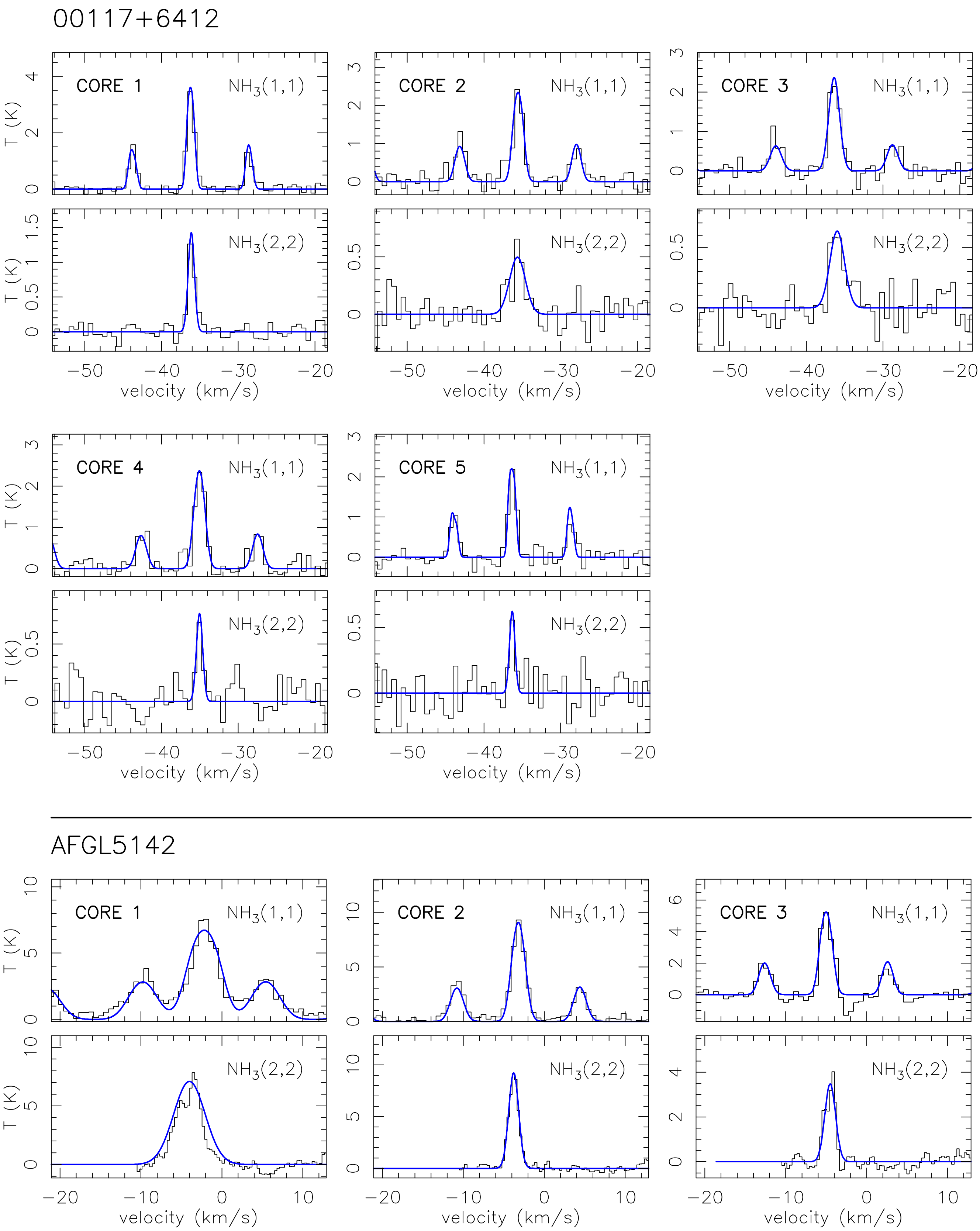

Figure B2. Observed (black histogram) and fitted (thick blue line) spectra of the NH$_3$ (1,1) and (2,2) lines for the cores listed in Table 3. Vertical axis corresponds to brightness temperature (in K), and horizontal axis corresponds to velocity (in km s^{-1}).

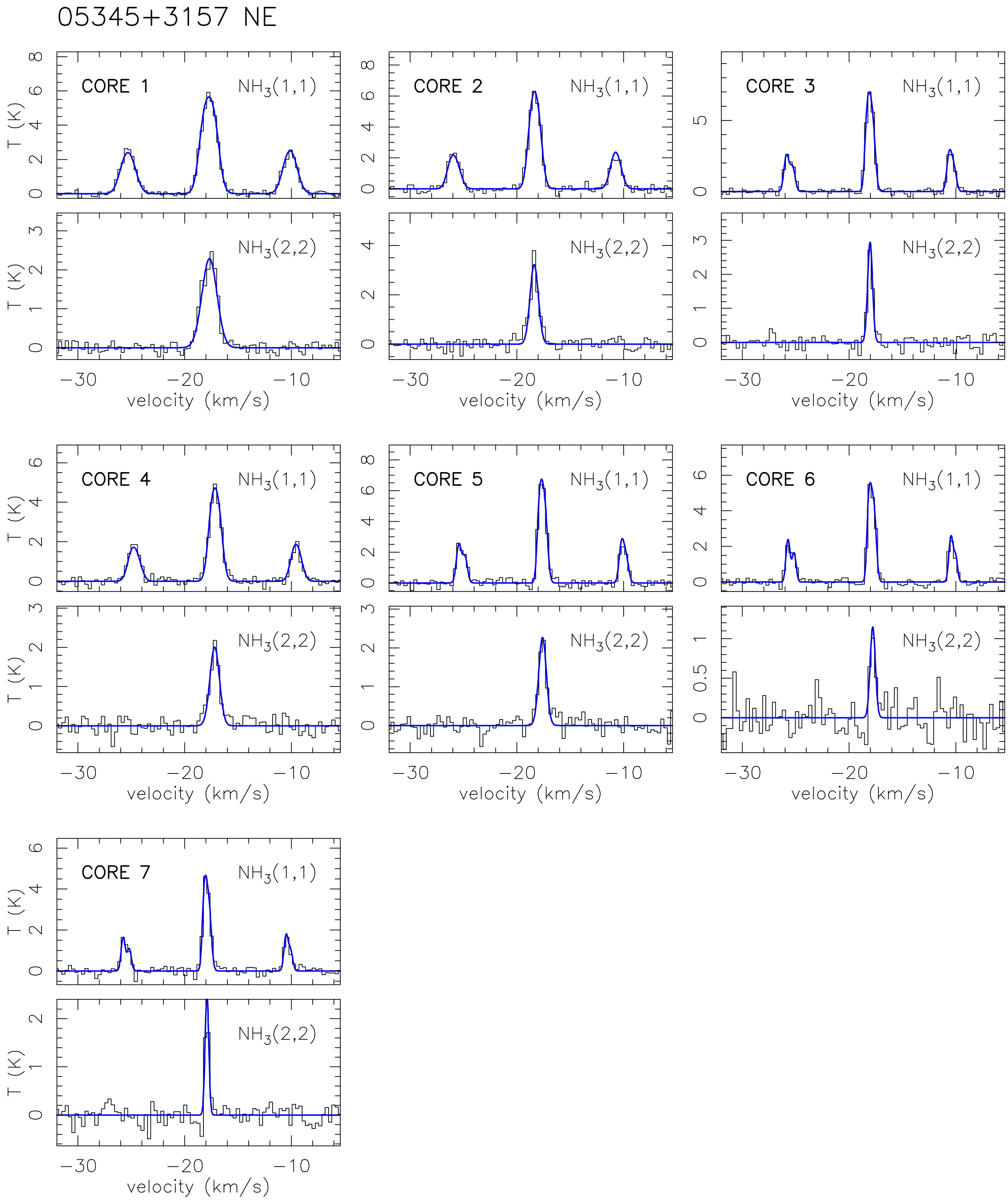

Figure B2 – *continued*

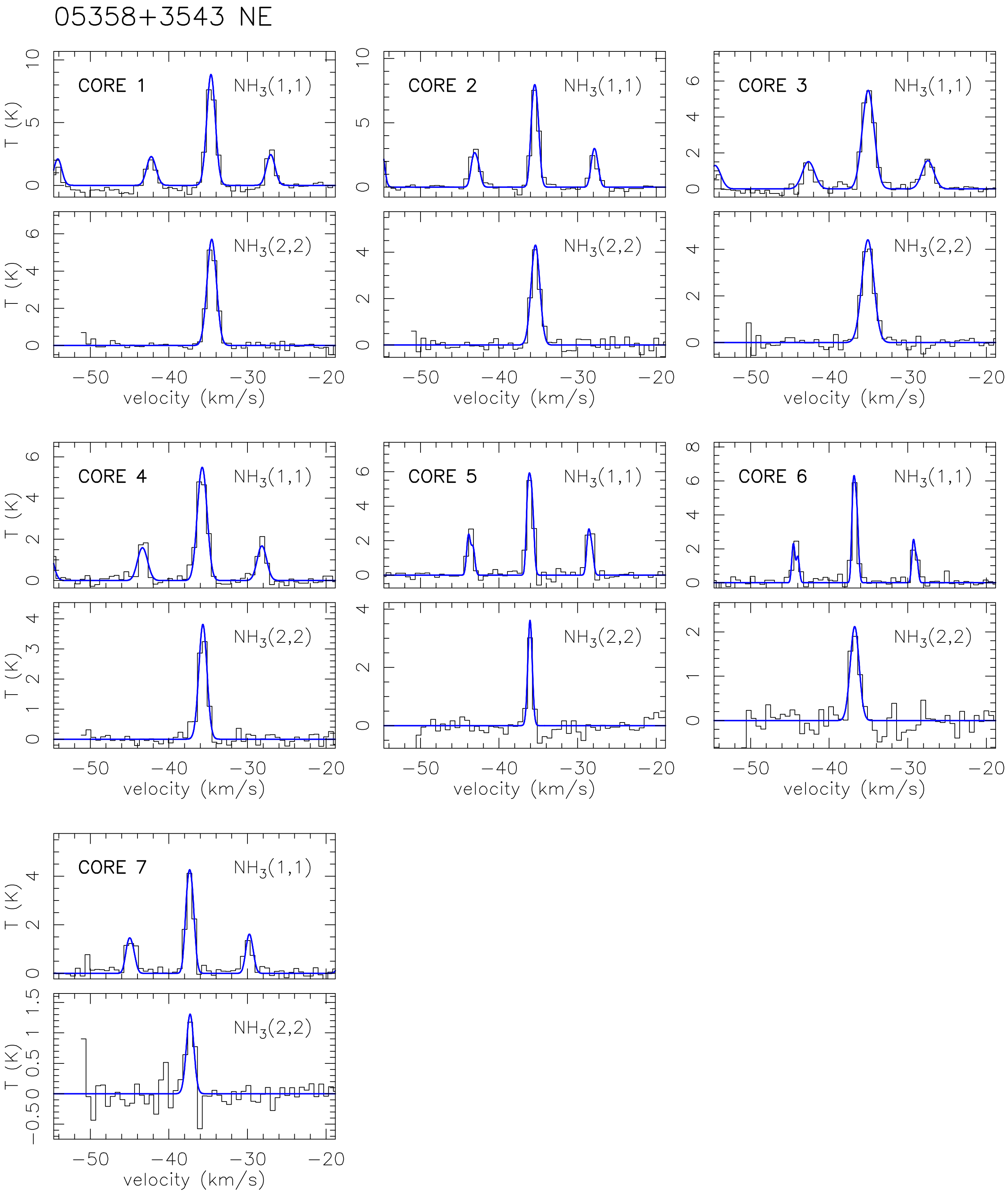

Figure B2 – *continued*

05373+2349

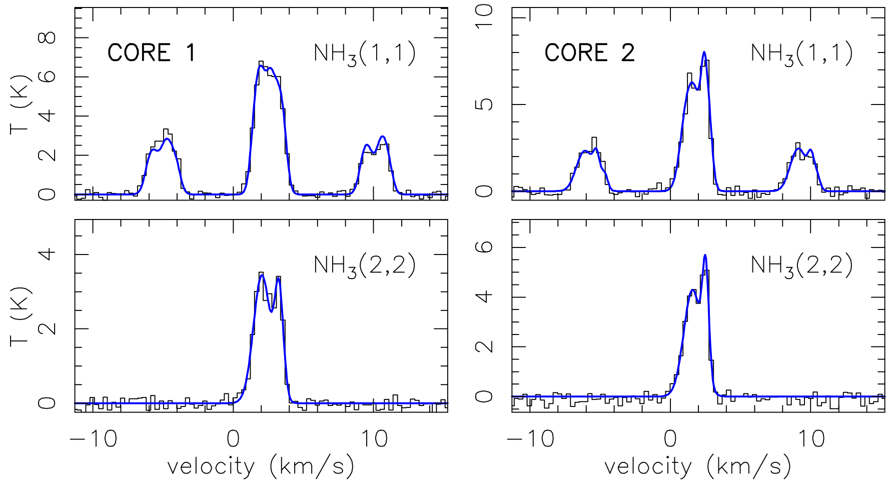

19035+0641

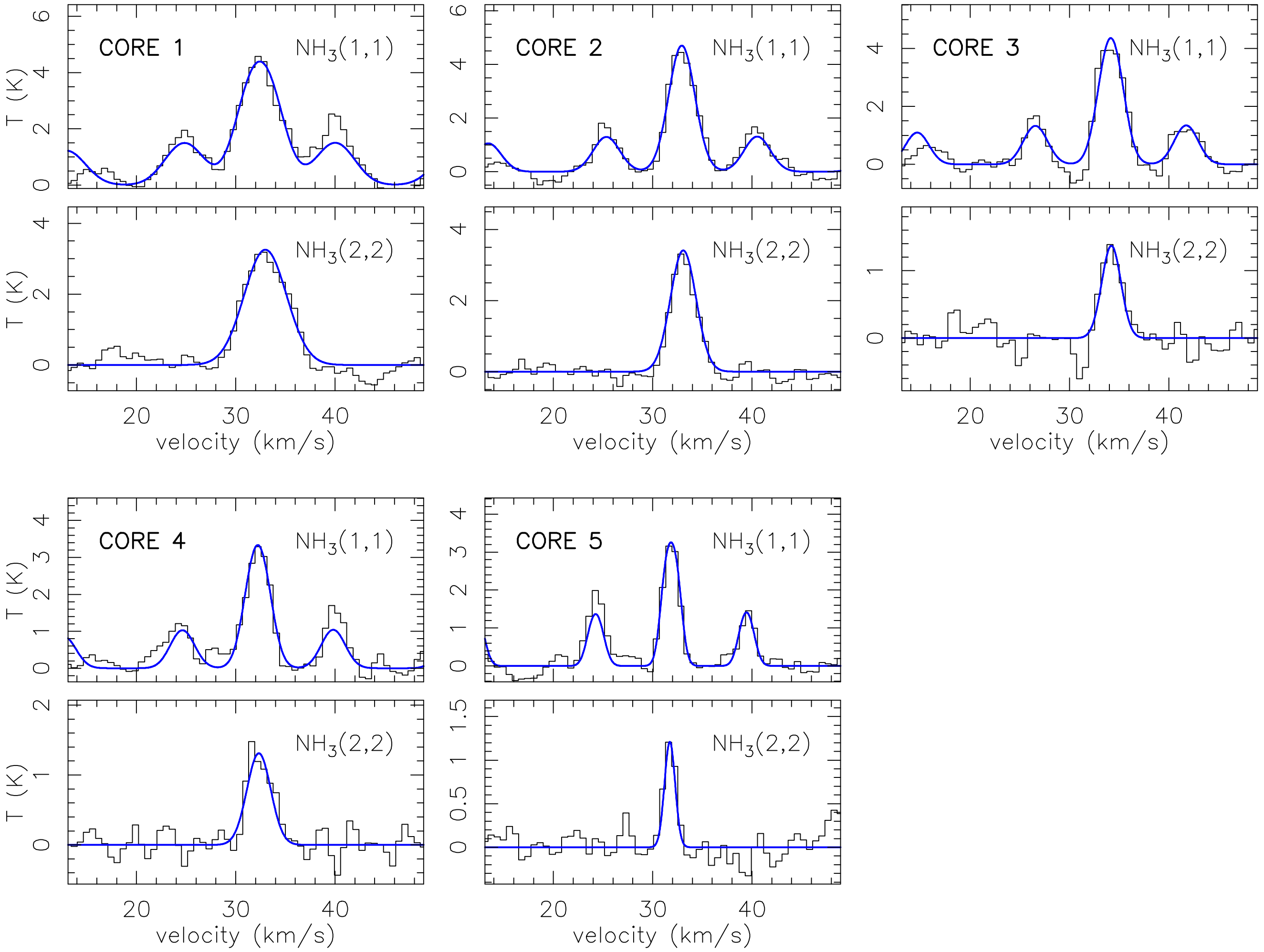

Figure B2 – *continued*

20081+3122

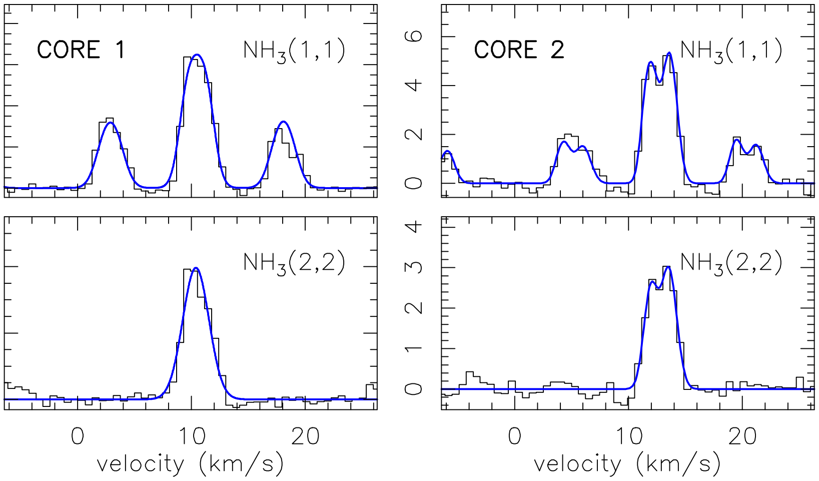

20126+4104

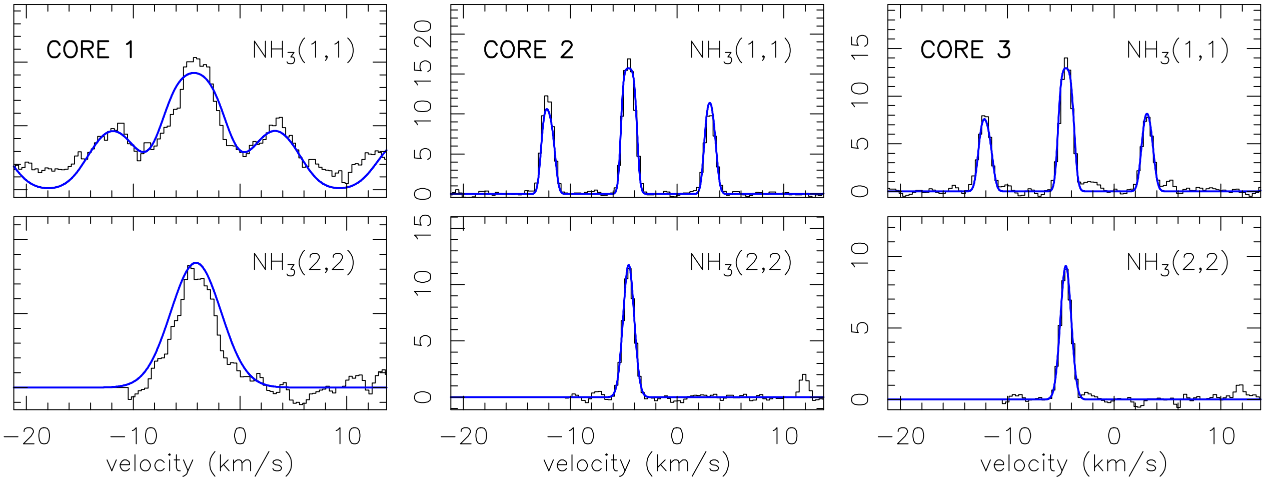

Figure B2 – *continued*

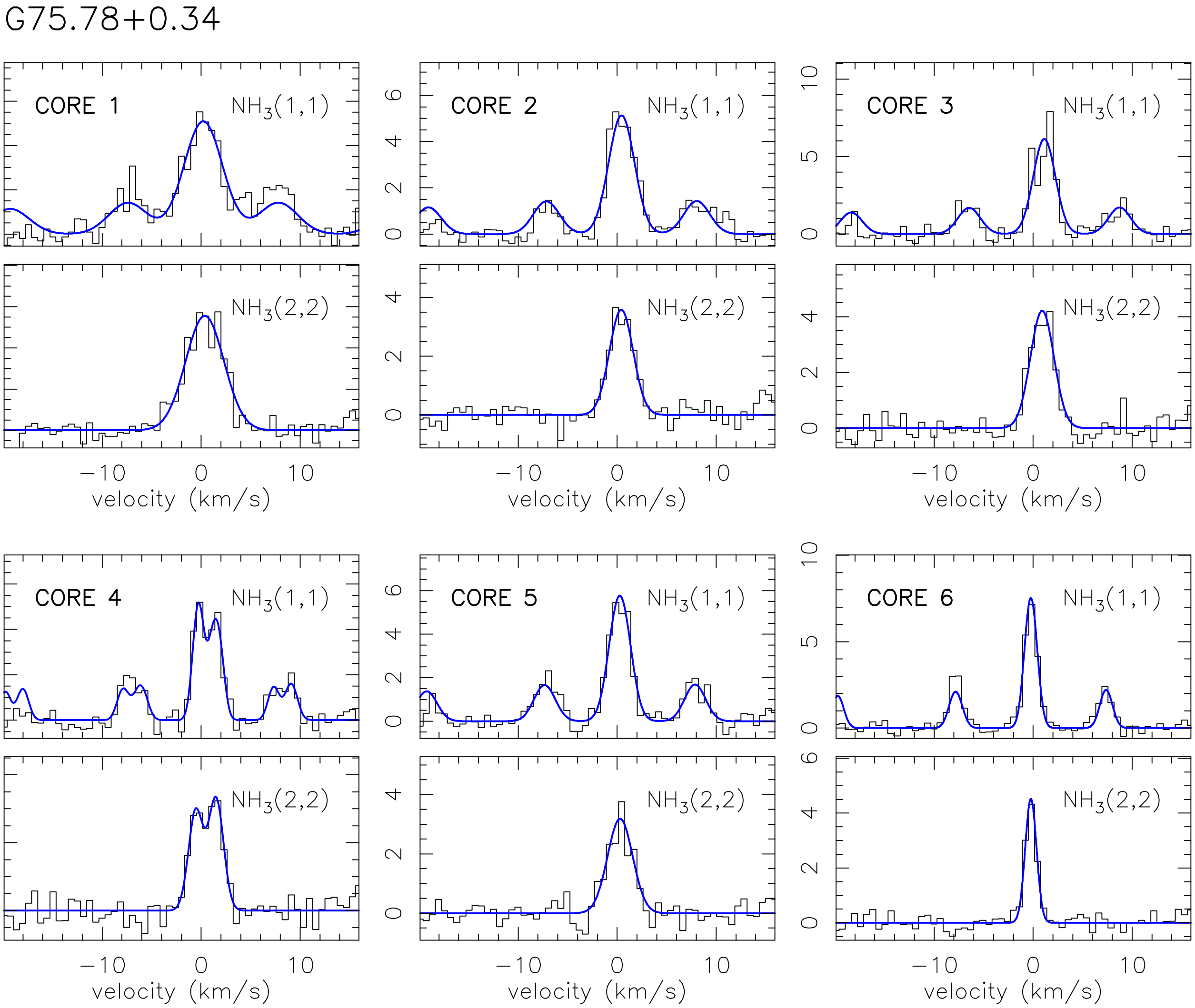

Figure B2 – *continued*

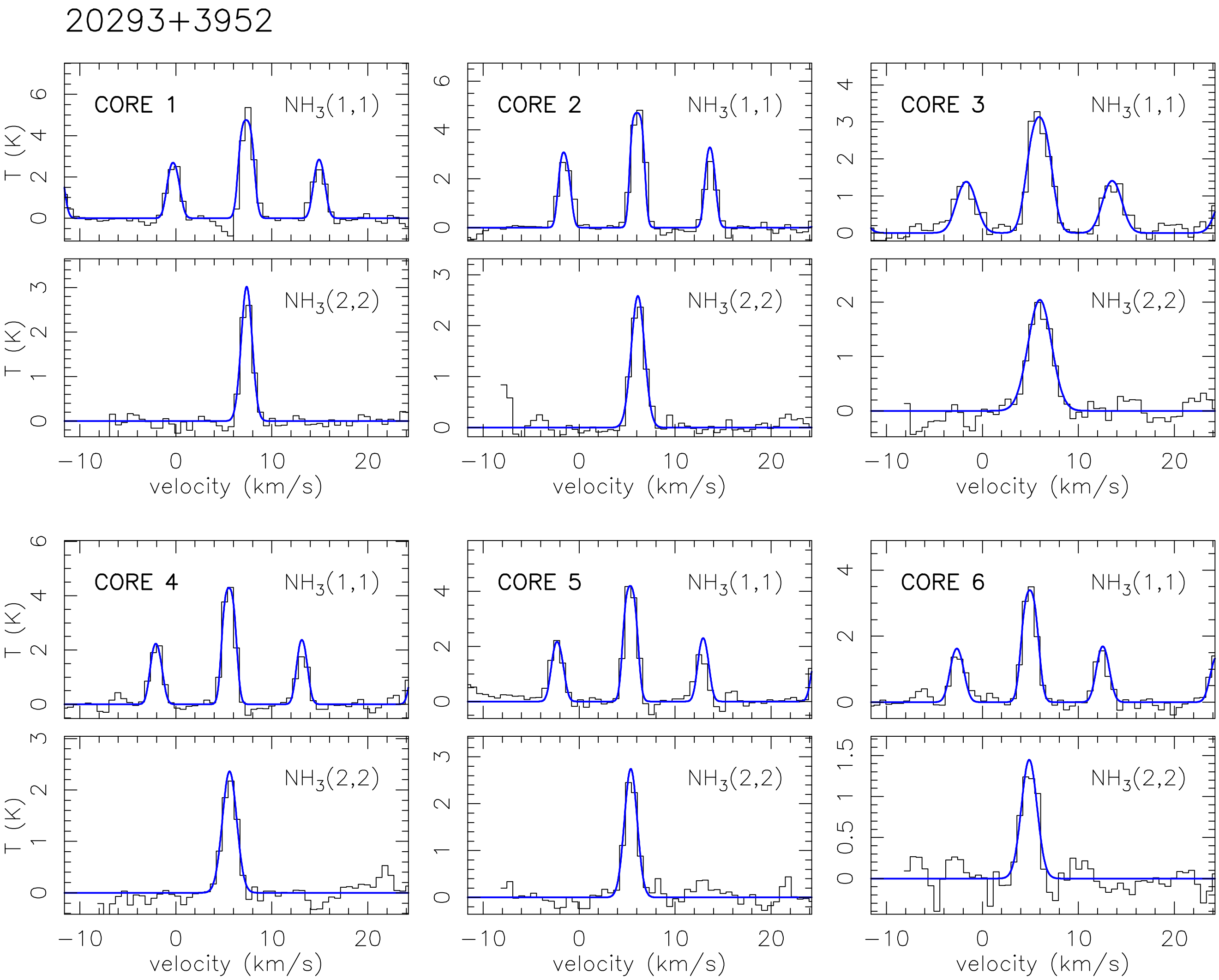

Figure B2 – *continued*

20343+4129

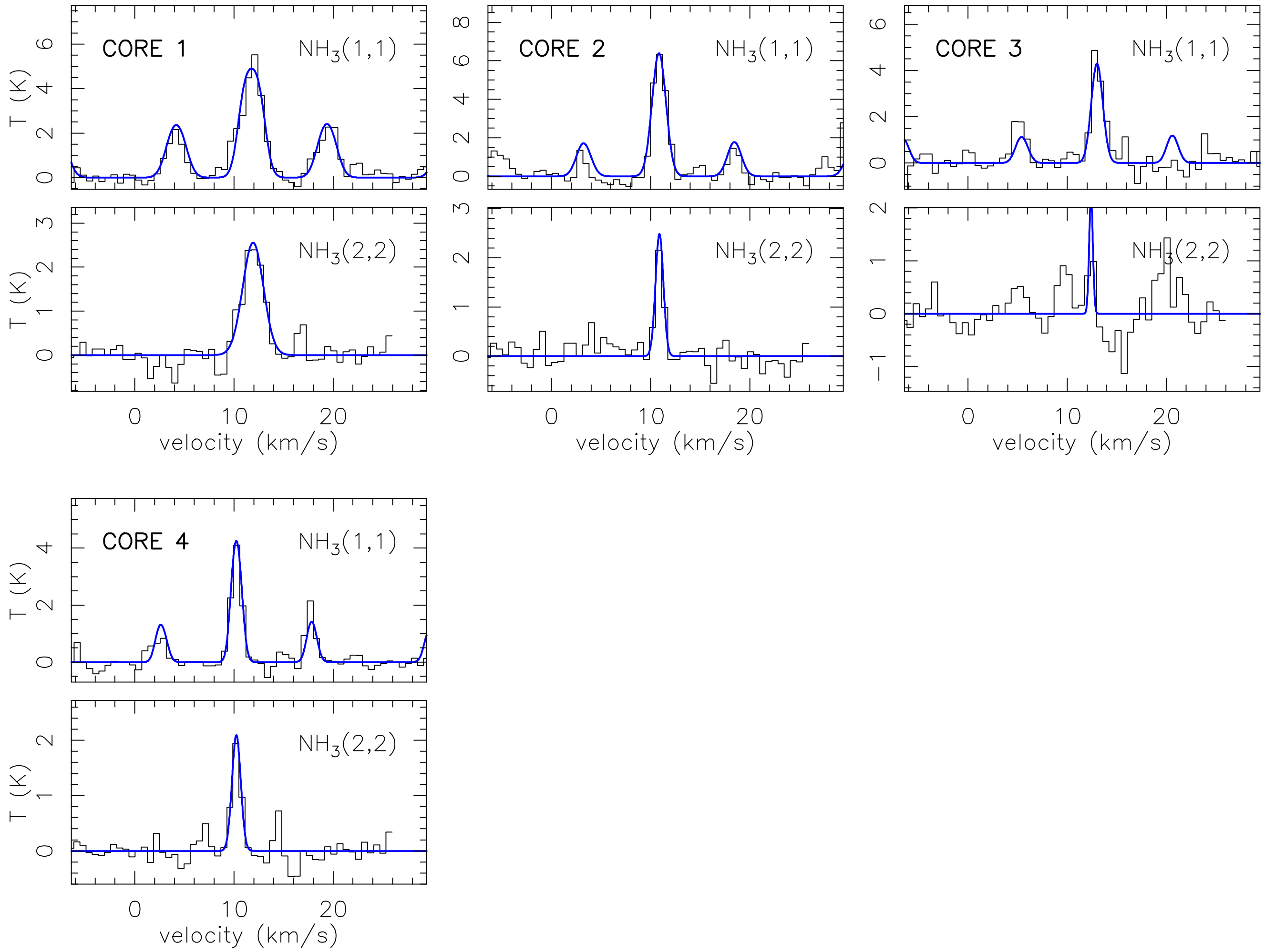

Figure B2 – *continued*

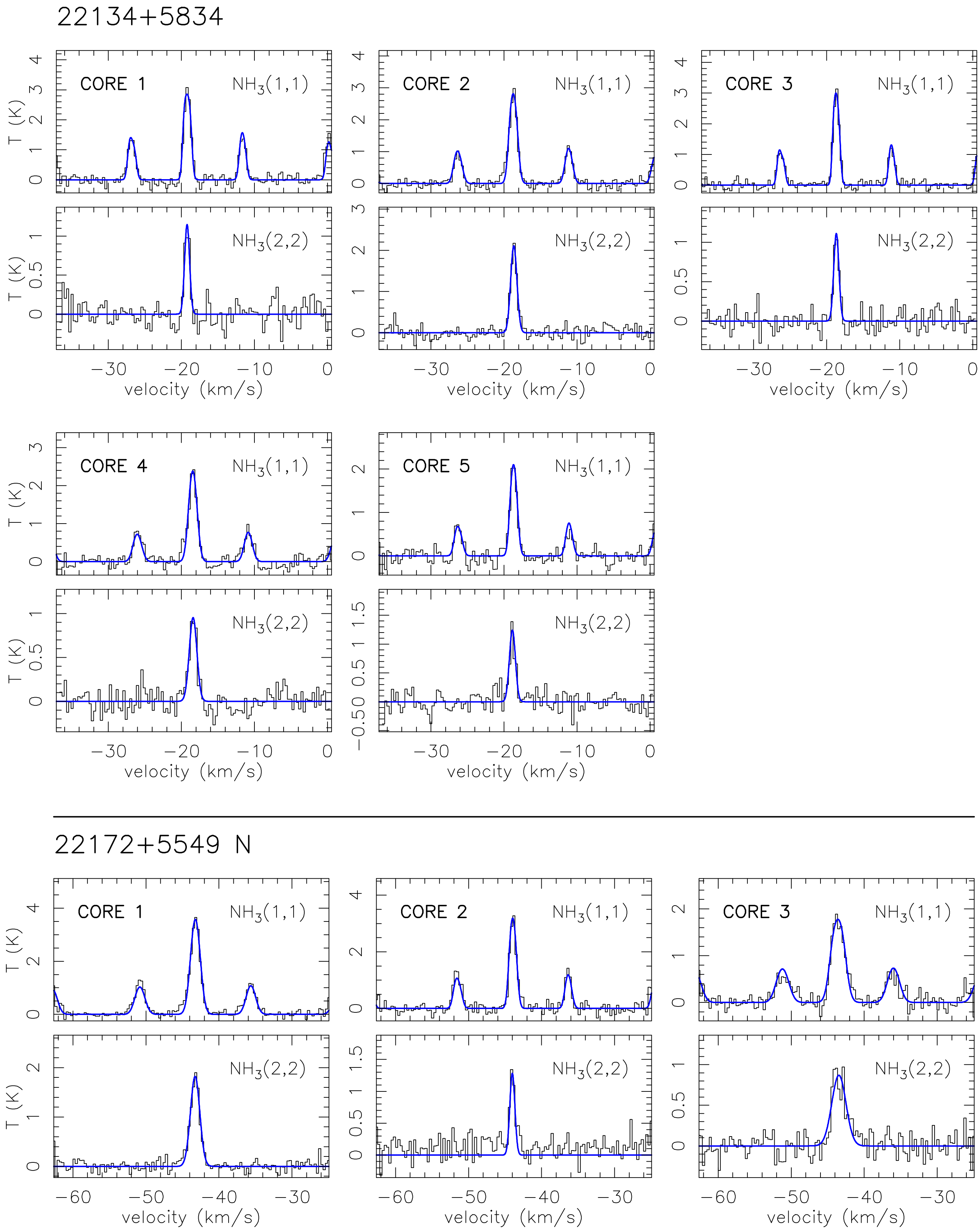
22134+5834

22172+5549 N

Figure B2 – *continued*

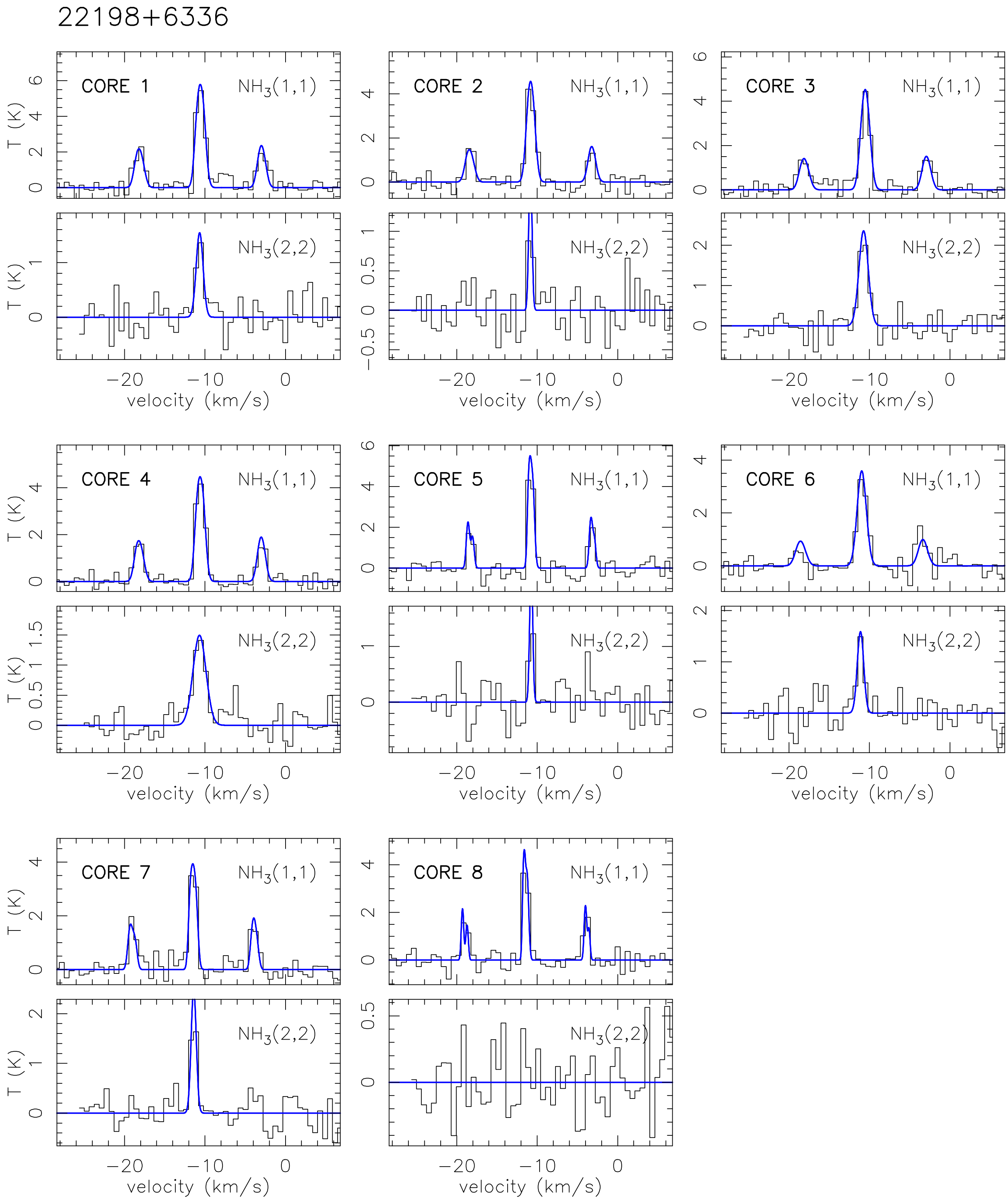

Figure B2 – *continued*

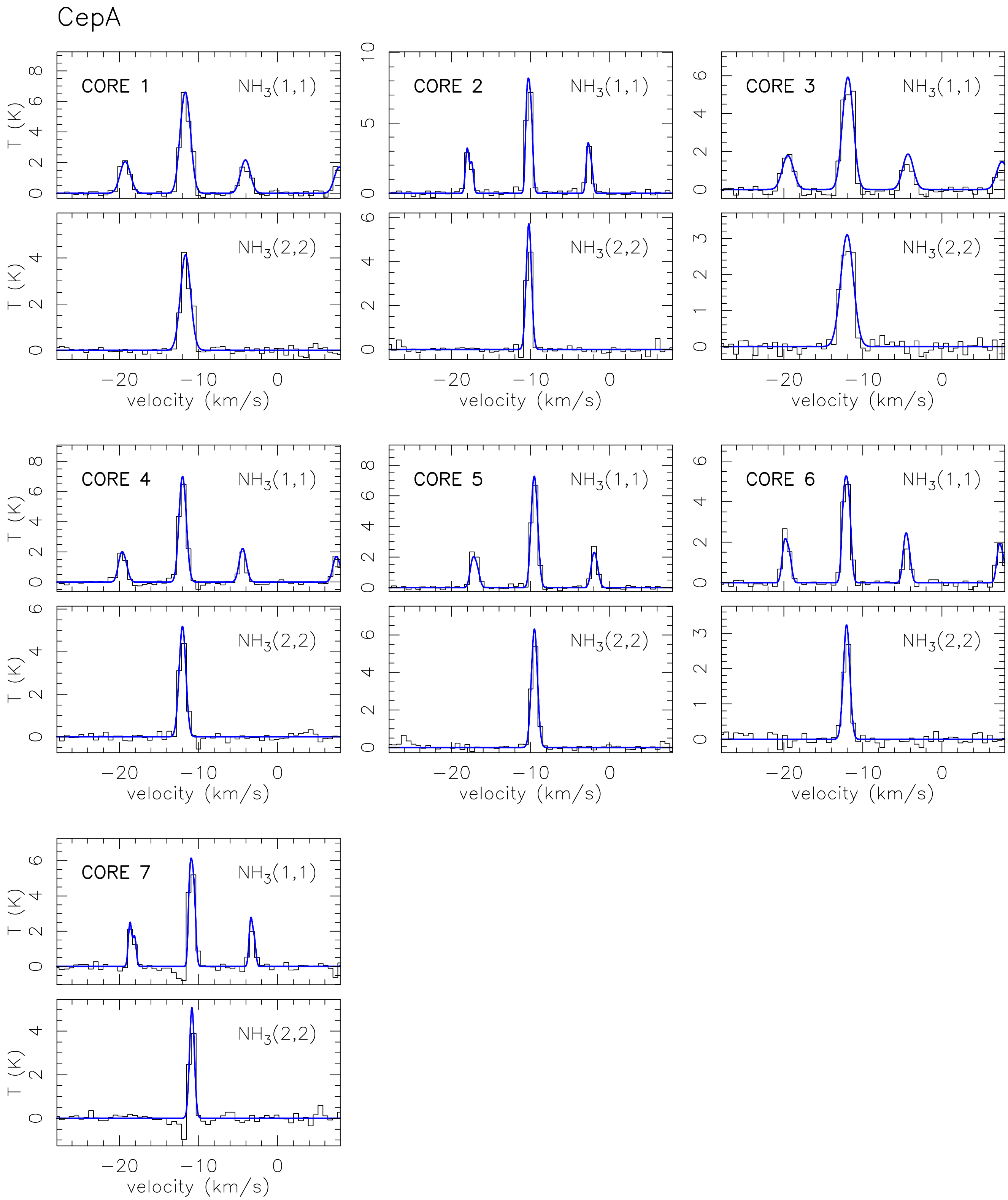

Figure B2 – *continued*